

THE CHEMICAL COMPOSITIONS AND EVOLUTIONARY STATUS OF RED GIANTS IN THE OPEN CLUSTER NGC 752

G. Böcek Topcu^{1,2*}, M. Afşar^{1,2}, M. Schaeuble², C. Sneden^{2,1}

¹*Department of Astronomy and Space Sciences, Ege University, 35100 Bornova, İzmir, Turkey;*

²*Department of Astronomy and McDonald Observatory, The University of Texas, Austin, TX 78712*

Accepted 2014 November 7

ABSTRACT

We present detailed chemical compositions of 10 red giant star members of the Galactic (open) cluster NGC 752, derived from high-resolution ($R \approx 60,000$), high signal-to-noise ($S/N \geq 140$) spectra. We confirmed cluster memberships by measuring the stellar radial velocities, and by deriving model atmosphere parameters (T_{eff} , $\log g$, $[\text{Fe}/\text{H}]$ and ξ_t) from equivalent widths of Fe I, Fe II, Ti I, and Ti II lines. The metallicity we obtained for NGC 752 ($[\text{Fe}/\text{H}] = -0.02 \pm 0.05$) is in good agreement with previous studies. We derived abundances of α (Mg, Si, Ca), light odd-Z (Na, Al), Fe-group (Sc, Ti, V, Cr, Mn, Fe, Co, Ni, Cu, Zn), n -capture (Y, La, Nd, Eu), and p -capture (Li, C, N, O) species for each star. Furthermore, we also derived abundances of the LiCNO p -capture element group and carbon isotopic ratios, using synthetic spectrum analyses of the Li I 6707 Å resonance doublet, the [O I] line at 6300 Å, the CH G-band features near 4311 and 4325 Å, the C₂ bandheads at 5160 and 5631 Å, and ^{12,13}CN red system lines in the 7995–8040 Å region. By applying recent isochrones to NGC 752 photometry, and comparing the color-magnitude diagram information to our Li abundances and ¹²C/¹³C ratios, we suggest that the 10 observed red giants can be separated into three first-ascent, six red-clump and one red horizontal branch star.

Key words: stars: abundances – stars: atmospheres. Galaxy: open clusters and associations: individual: NGC 752

1 INTRODUCTION

Open clusters (OCs) are excellent probes to investigate both stellar and Galactic disk evolution. According to classical theories, OCs members were formed from the same proto-cluster cloud at the same time and the same distance. This lends particular importance to the morphology of an OC color-magnitude diagram (CMD), as it allows determination of the temperatures, luminosities, and evolutionary states of cluster members more accurately than can be done for field stars.

All members of individual OCs should have comparable initial chemical compositions, differing only in their initial masses. As predicted by the models, the individual nucleosynthesis and mixing histories of the members are responsible for any surface abundance differences among evolved OC stars. In classical stellar evolution, the so-called first dredge-

up, which occurs at the base of the red giant branch (RGB)¹, is the main mechanism that changes the surface abundances. The best indicators of this mixing are the observed changes in abundances of the elements susceptible to proton-capture mechanisms. In stars with masses and metallicities similar to the sun, photospheric abundances of ¹²C and ¹²C/¹³C will decrease while the abundances of He (unobservable), ¹³C and ¹⁴N will increase. Surface Li abundances vary greatly from one star to the next, and on average will also greatly decrease during the star's evolution from main sequence to the RGB phase.

The quantitative changes in LiCNO abundances depend on the initial masses and metallicities of the stars (e.g. Sweigart et al. 1989; Charbonnel 1994; Boothroyd & Sackmann 1999; Marigo 2001). For example, standard predictions suggest that ¹²C/¹³C = 20 to 30 is typ-

* E-mail: gamzebocek@gmail.com (GBT); melike.afsar@ege.edu.tr (MA); mschaeu@astro.as.utexas.edu (MS); chris@verdi.as.utexas.edu (CS)

¹ In this paper we will use the term red giant (RG) generically, meaning all cool and luminous stars; RGB will designate stars on the first ascent of the giant branch; and RC will designate He-burning red clump stars.

ical for RGB stars (e.g. Iben 1967; Dearborn et al. 1976), though observations yield a more complex answer. In particular, early spectroscopic studies (e.g. Tomkin et al. 1975, 1976; Lambert & Ries 1981; Sneden et al. 1986) showed that RGB and RC stars often exhibit $^{12}\text{C}/^{13}\text{C} < 15$, much lower than expected.

Gilroy (1989, hereafter Gil89) found a strong anti-correlation between stellar mass and $^{12}\text{C}/^{13}\text{C}$ ratios in clusters with turnoff masses $M < 2.2 M_{\odot}$. This trend could not be explained by canonical stellar evolution models without invoking some sort of extra convective envelope mixing. Recently, Afşar et al. (2012) have discovered anomalously low $^{12}\text{C}/^{13}\text{C}$ ratios among metal-rich thin-disk field red horizontal branch stars, indicating that their carbon isotope ratios may have been altered during RGB evolution. Several extra-mixing processes have been suggested to explain these low isotopic ratios, e.g., Sweigart & Mengel (1979); Charbonnel (1994); Charbonnel et al. (1998); Boothroyd & Sackmann (1999); Charbonnel & Lagarde (2010). For first-ascent RGB stars with $M < 2.2 M_{\odot}$, especially at low metallicities, both $^{12}\text{C}/^{13}\text{C}$ and C/N ratios sharply drop at the so-called “luminosity function bump” (Gratton et al. 2000). At this evolutionary stage, the outward-advancing H-burning shell cancels out the chemical discontinuity left by the convective envelope, allowing further mixing to take place (e.g. Charbonnel 1994).

The observational challenge is to discern the results of the extra-mixing processes through the abundances in stars with well-determined masses and luminosities. This is difficult for field stars, since it is not easy to determine their masses. However, mass estimation is easily done for open and globular cluster RGs. Detailed studies of LiCNO abundances of evolved members of individual OCs are increasing (e.g., Gilroy 1989; Gilroy & Brown 1991; Luck 1994; Tautvaišienė et al. 2000; Tautvaišienė et al. 2005; Smiljanic et al. 2009; Mikolaitis et al. 2010, 2011a,b, 2012). In this paper we aim to add to this growing literature by presenting high-resolution spectral analyses of NGC 752 RG member stars. We report atmospheric parameters, $[\text{Fe}/\text{H}]$ metallicities², relative abundances and ratios of elements belonging to the α , light odd-Z, Fe-peak, and neutron-capture groups, with a particular focus on the LiCNO group. We employ new, comprehensive laboratory transition studies of CH, C₂, and CN molecular bands, which have materially increased the reliability of proton-capture abundances derived in RG stars.

The structure of this paper is as follows: in §2 we introduce NGC 752 and its RGB members. The observations and reductions are outlined in §3. We discuss compilation of atomic/molecular line lists and equivalent width measurements in §4. The derivation of model atmospheric parameters is described in §5, followed by abundance analysis in §6. Finally, in §7 we discuss the implications of our results for the evolution of NGC 752.

Table 1. NGC 752 cluster parameters.

Quantity	Value	Ref.
Right Ascension (2000)	01 57 41	WEBDA
Declination (2000)	+37 47 06	WEBDA
Galactic longitude	137.125	WEBDA
Galactic latitude	−23.254	WEBDA
Distance	447 pc	Dan94
$E(B - V)$	0.035	Dan94
$(m - M)_0$	8.25	Dan94
Age	1.7 to 1.9 Gyr	Dan94
Turnoff Mass	1.5 M_{\odot}	Bartašiūtė et al. (2007)

2 NGC 752 AND ITS RG STARS

NGC 752 is one of the closest ($\simeq 447$ pc, Daniel et al. 1994, hereafter Dan94) intermediate age (1–2 Gy) OCs. Due to its age and distance, NGC 752 has been the focus of many photometric and spectroscopic studies for nearly a century. Basic parameters of this cluster are given in Table 1. We will elaborate on some of these quantities below.

Photographic observations and member identifications of NGC 752 were first made by Heinemann (1926). Ebbighausen (1939) conducted the initial proper motion study of this cluster and also expanded the membership identifications of Heinemann (1926). Using new stellar identification systems, the membership of several other stars in NGC 752 has been established. Mermilliod et al. (1998) summarized past numbering systems for the RG members of NGC 752 and confirmed the membership of 15 of these stars. Four of them have been reported as spectroscopic binaries and were thus not included in our sample. Later, Mermilliod et al. (2008, hereafter Mer08), using the Heinemann (1926) numbering system, introduced a new naming system that we have adopted through this study, using the prefix “MMU”.

Mermilliod et al. (1998) concentrated on the binary frequency and the RG branch morphology of NGC 752. Investigating the color-magnitude diagram (CMD) of the cluster, they discovered an unusual distribution of RGB stars. They showed that although the RGs nominally occupy the so-called He-burning clump domain, some of them were fainter and bluer than true clump members ought to be. Girardi et al. (2000) investigated this unusual morphology in NGC 752 and NGC 7789, which has a similar red clump distribution. They suggested that the peculiar distribution can occur if OCs have He-burning stars with a significant mass spread at the same time. The lower-mass stars would have undergone standard He-flash prior to settling in the clump, while the higher-mass stars would have ignited helium quiescently. They also suggested that the dispersion in red clump masses might have been caused by different amounts of mass-loss that had taken place during the RGB phase.

Detailed abundance analysis of individual RC members in this cluster began with Pilachowski et al. (1988), who investigated the lithium abundances of evolved stars in NGC 752 and M 67 using the Li I 6707 Å resonance doublet. They observed 24 RGs in the vicinity of NGC 752 and reported Li abundances for 11 members previously identified by Heinemann (1926). Among those, only Heinemann

² For elements A and B, $[\text{A}/\text{B}] = \log (N_{\text{A}}/N_{\text{B}})_{\star} - \log (N_{\text{A}}/N_{\text{B}})_{\odot}$ and $\log \epsilon(\text{A}) = \log (N_{\text{A}}/N_{\text{H}}) + 12.0$. Also, metallicity will be taken to be the $[\text{Fe}/\text{H}]$ value.

77 and 208 yielded strong Li features with abundances of $\log\epsilon(\text{Li}) = 1.1$ and 1.4 , respectively. These stars were thus interpreted as first-ascent giants, while the rest of the observed members were identified as evolved He-burning clump stars. As mentioned in §1, Gil89 reported high-resolution spectral analyses of C isotopic ratios from CN features near 8004 \AA and new Li abundances in selected RGB members of 19 clusters. In the lower turnoff mass OCs of her sample, a clear correlation between cluster turnoff mass and $^{12}\text{C}/^{13}\text{C}$ was found. The prior results for NGC 7789 (Pilachowski 1986, Sneden & Pilachowski 1986) fit in with the general trend; see Gil89 Figure 9.

Interpretations of NGC 752 RG evolutionary states depend on fundamental cluster parameters such as distance modulus, reddening, age, main-sequence turnoff mass, and metallicity. Here we summarize the literature values of these quantities, noting that estimates of $(m - M)_0$, $E(B - V)$, age, M_{TO} , and $[\text{Fe}/\text{H}]$ have not significantly changed from earliest investigations to the present time.

Reddening and Distance Modulus: In the publication history of NGC 752, most of the methods for deriving these quantities have been applied to its main sequence members. Dan94 collected the data of six photometric systems and transformed them to the Johnson UBV system. They derived $E(B - V) = 0.035 \pm 0.005$ and $(m - M)_0 = 8.25 \pm 0.10$ (447 ± 10 pc). Bartašiūtė et al. (2007) conducted seven-color Vilnius photometry for NGC 752, and from the best isochrone match to the CMD they found $(m - M)_0 = 8.06 \pm 0.03$ (409 ± 6 pc). Later, Bartašiūtė et al. (2011) analyzed Vilnius multicolor photometry of NGC 752 with an expanded sample that extended down the main sequence to $V \cong 18.5$. Using the data of 70 photometric members, they derived $(m - M)_0 = 8.37 \pm 0.32$ (472 ± 72 pc), consistent with their prior estimate due to its larger uncertainty.

Cluster Age and Main Sequence Turnoff Mass: These quantities have been determined by comparing the NGC 752 photometry to isochrones. Dan94 derived an age of 1.9 ± 0.1 Gyr from matching classical isochrones, and 1.7 ± 0.1 Gyr from isochrones that included convective overshooting. The isochrone matches to Vilnius-system photometry yielded an age of 1.58 ± 0.04 Gyr (Bartašiūtė et al. 2007) and 1.41 Gyr (Bartašiūtė et al. 2011). The cluster turnoff mass Bartašiūtė et al. (2007) suggest $M_{TO} \approx 1.5 M_{\odot}$, while Gil89 estimated a turn off mass $M_{TO} \approx 1.6 \pm 0.13 M_{\odot}$ using photometric data then available.

Metallicity: Since metallicity is one of the most important parameters in the evolution of OCs, several NGC 752 studies have been devoted to this parameter. Like most OCs, its metallicity is approximately solar. Nevertheless, a variety of photometric and spectroscopic techniques have been applied to derive the $[\text{Fe}/\text{H}]$ value more accurately. Dan94 used both spectroscopic and photometric approaches to derive a mean cluster metallicity of $[\text{Fe}/\text{H}] = -0.15 \pm 0.05$. From Vilnius photometry, Bartašiūtė et al. (2007) derived $\langle [\text{Fe}/\text{H}] \rangle = -0.12 \pm 0.03$, and Bartašiūtė et al. (2011) revised this value to $\langle [\text{Fe}/\text{H}] \rangle = +0.16 \pm 0.09$. Pöhl & Paunzen (2010) developed a statistical method to determine OC metallicities, finding $\langle [\text{Fe}/\text{H}] \rangle = +0.05$. Paunzen et al. (2010) derived $\langle [\text{Fe}/\text{H}] \rangle = -0.15 \pm 0.11$ by using the previously published photometric data sets of the cluster. Anthony-Twarog & Twarog (2006) reported Strömgen photometry for 7 RG and 21 main-sequence stars

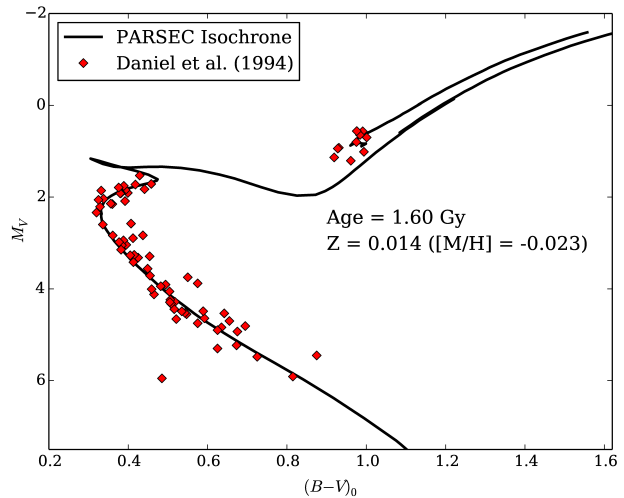


Figure 1. The CMD of the OC NGC 752 with PARSEC isochrones (Bressan et al. 2012).

of NGC 752, and from 10 non-binary members they derived $[\text{Fe}/\text{H}] = -0.06 \pm 0.03$. Finally, Heiter et al. (2014) reported a mean metallicity of $\langle [\text{Fe}/\text{H}] \rangle = -0.02 \pm 0.04$, based on spectroscopic data gathered from 19 different sources. There are two recent studies with detailed high-resolution spectral analyses of NGC 752. Based on four RGBs, Carrera & Pancino (2011, hereafter Car11) determined a mean cluster metallicity of $\langle [\text{Fe}/\text{H}] \rangle = 0.08 \pm 0.04$. Reddy et al. (2012, hereafter Red12) have reported a value $\langle [\text{Fe}/\text{H}] \rangle = -0.02 \pm 0.05$ also from four RGBs, but only one is common with the sample of Car11. We conclude that a cluster metallicity of $[\text{Fe}/\text{H}] \sim 0.0$ is a reasonable summary of past metallicity investigations.

For this study, we have adopted reddening, distance modulus, and age of NGC 752 from Dan94; see Table 1. Fortunately, the above discussion suggests that the important cluster quantities are generally agreed upon by all the literature studies of NGC 752. For the NGC 752 turnoff mass (also quoted in Table 1), we have adopted the value from Bartašiūtė et al. (2007), which is one of the most recent, complete, and internally-consistent photometric studies of NGC 752.

2.1 Colour–Magnitude diagram

The CMD of NGC 752 has been studied by several authors (e.g. Dan94, Bartašiūtė et al. 2007 and Bartašiūtė et al. 2011). We used the combined photometric data from Dan94, since the data from Bartašiūtė et al. (2007) and Bartašiūtė et al. (2011) do not include all the NGC 752 RG members present in our target list (Table 2).

Figure 1 shows a comparison of the photometric data obtained by Dan94 to the latest set of PARSEC isochrones (Bressan et al. (2012)). Earlier studies of NGC 752 employed isochrones published by VandenBerg et al. (2006), Meynet et al. (1993) and Castellani et al. (1992) to obtain metallicity and age estimates of this cluster. However, several important physical considerations, such as convective overshooting, which might be important for age estimation in intermediate-age OCs such as NGC 752, have been neglected in these older calculations. Additionally, old opacity

Table 2. Observed NGC 752 RGs. Coordinates, K magnitudes and proper motions are taken from Simbad database. B and V magnitudes are from Dan94.

Star	Other Name	RA (2000)	DEC (2000)	<i>B</i>	<i>V</i>	<i>K</i>	μ_α (mas/yr)	μ_δ (mas/yr)
Cluster Members								
MMU 1	BD+37 407	01 55 12.616	+37 50 14.54	10.31	9.39	7.23	3.4	−10.8
MMU 3	BD+37 408	01 55 15.292	+37 50 31.29	10.41	9.47	7.20	11.3	−11.3
MMU 11	BD+37 409	01 55 27.669	+37 59 55.25	10.17	9.34	7.04	8.7	−13.2
MMU 24	BD+37 412	01 55 39.370	+37 52 52.49	9.88	8.90	6.55	7.5	−13.7
MMU 27	BD+36 350	01 55 42.387	+37 37 54.55	10.13	9.17	6.80	6.9	−10.3
MMU 77	BD+36 358	01 56 21.634	+37 36 08.37	10.54	9.43	6.92	4.8	−14.8
MMU 137	BD+37 424	01 57 03.110	+38 08 02.62	9.89	8.89	6.64	8.7	−12.9
MMU 295	BD+37 441	01 58 29.820	+37 51 37.60	10.23	9.29	7.04	9.4	−10.3
MMU 311	BD+37 448	01 58 52.903	+37 48 57.23	10.07	9.04	6.64	9.75	−11.1
MMU 1367	BD+37 450	01 59 14.800	+38 00 55.31	10.02	8.99	6.65	10.9	−9.6
Non Members								
MMU 39	BD+37 415	01 55 54.759	+37 52 00.18	9.05	8.09	5.77	−1.3	−11.3
MMU 215	BD+36 370	01 57 42.736	+37 40 11.35	8.35	7.12	4.45	15.0	−32.5

data (Rogers & Iglesias 1992; Maeder & Meynet 1991) was used in the calculations of the final isochrone tracks.

PARSEC isochrones are calculated using not only two different types of overshooting (core convective & envelope), but also two different types of opacities. For the high temperature regime, OPAL 1996 (Iglesias & Rogers 1996) data is used in the computation, while the low temperature opacities are obtained from the AESOPUS code (Marigo & Aringer 2009). This ensures that isochrone tracks for *any* given input chemical composition can be calculated. In addition to these improvements, the equations of state were calculated from the latest version of the freely available FREEEOS³ package. The combination of these updated parameters and input physics should yield more reliable isochrones and thus also age and metallicity estimates.

To obtain our final estimates of the age and metallicity of this cluster, an iterative fit of the PARSEC isochrones to the photometric data was done. The final results can be seen in Figure 1. Our results are in good agreement with those obtained by previous studies, indicating that the choice of the isochrone source is not important. The final input parameters of our isochrone are $Z = 0.014$ and an age of 1.6 Gyrs. These lead to a turnoff mass of $M_{TO} \approx 1.6M_\odot$, again in good agreement with all previous studies.

2.2 RG target selection

To assemble the NGC 752 sample we began with the the OC database WEBDA⁴, selecting stars labeled as RGs in its V versus $B - V$ CMD. We checked the membership status of these stars using the OC RG radial velocity (RV) survey of Mer08. In that paper, velocities were reported from the COROVEL “spectrovelocimeter” observations of 1309 potential members of 166 clusters. Mer08 surveyed 30 possible members of NGC 752, finding just 10 stars without obvious spectroscopic binary companions and with RVs close to the cluster mean of $\langle RV \rangle = +5.04 \pm 0.08 \text{ km s}^{-1}$ (standard deviation of the sample $\sigma = 0.32 \text{ km s}^{-1}$). We gathered

spectra of these 10 stars. We also observed two suspected non-member stars from their list to test whether we could rule out their NGC 752 membership from our data alone. Our target RGs are listed in Table 2, giving identifications in the MMU (Mer08) and BD systems. Table 2 also lists RA, DEC, and proper motions values taken from the SIMBAD⁵ database, B and V magnitudes from Dan94, and K magnitudes from the 2MASS survey (Skrutskie et al. 2006). All of our programme stars are bright ($V < 9.47$), thus easily accessible to high-resolution spectroscopy.

3 OBSERVATIONS AND REDUCTIONS

High resolution spectra of the NGC 752 targets were gathered with the Robert G. Tull Cross-Dispersed Echelle spectrograph (Tull et al. 1995) on the 2.7 m Harlan J. Smith Telescope at McDonald Observatory. The wavelength range of the spectra was 4000 to 8000Å with a resolving power of $R \equiv \lambda/\Delta\lambda \approx 60,000$. The spectral order coverage of this setup is continuous up to $\lambda \simeq 5700 \text{ Å}$, but has small gaps between the echelle orders as the orders stretch in length at longer wavelengths. In Table 3 we list the observation dates and exposure times for each of our target stars. Three exposures per target were taken at each night. Exposure times given in Table 3 give the time for a single exposure.

We reduced the data by using standard IRAF⁶ tasks in the *ccdred* package, including bias subtraction, flat-fielding, and scattered light subtraction. Then, the spectra were extracted by using tasks in the *echelle* package. Th-Ar comparison lamp exposures taken at the beginning and end of each night were used for wavelength calibration. To filter out cosmic-ray and other single-exposure anomalies, we combined all available integrations for each star. In combination with the IRAF *telluric* task, we used the spectrum of a hot, rapidly rotating star to remove telluric line contamination (O_2 and H_2O) from our target spectra.

Our target stars are solar-metallicity RGs and, as such,

³ <http://freeeos.sourceforge.net/>

⁴ <http://www.univie.ac.at/webda/webda.html>

⁵ <http://simbad.u-strasbg.fr/simbad/>

⁶ <http://iraf.noao.edu/>

Table 3. Observing logs and radial velocities of the observed stars.

Star	Obs. Date	Exp. (s)	S/N	RV^a ($km\,s^{-1}$)	RV^b ($km\,s^{-1}$)	RV^c ($km\,s^{-1}$)	RV^d ($km\,s^{-1}$)
Cluster Members							
MMU 1	2012 November	3600	160	4.73 ± 0.20	5.19 ± 0.15	5.49 ± 0.44	
MMU 3	2012 November	3600	150	4.11 ± 0.20	4.56 ± 0.10		
MMU 11	2012 November	3600	175	4.45 ± 0.19	4.75 ± 0.12		
MMU 24	2012 October	3600	185	4.86 ± 0.19	5.36 ± 0.10		
MMU 27	2012 November	3600	190	4.39 ± 0.19	4.58 ± 0.11		
MMU 77	2012 November	3600	155	4.58 ± 0.20	5.02 ± 0.09		6.3 ± 0.2
MMU 137	2012 October	1350	170	5.59 ± 0.20	5.25 ± 0.09		5.9 ± 0.2
MMU 295	2014 February	2700	140	6.32 ± 0.23	5.20 ± 0.09		6.3 ± 0.2
MMU 311	2012 October	2700	180	5.19 ± 0.19	5.79 ± 0.09	6.00 ± 0.30	6.7 ± 0.2
MMU 1367	2012 October	2700	210	3.98 ± 0.19	4.55 ± 0.11		
Non Members							
MMU 39	2012 October	3600	180	-21.05 ± 0.20	-21.67 ± 0.14		
MMU 215	2012 October	1800	290	9.51 ± 0.24	9.29 ± 0.13		

^a This study.

^b Mermilliod et al. (2008).

^c Carrera & Pancino (2011).

^d Reddy et al. (2012).

have very line-rich spectra. Pure continuum regions stretching more than about half an Ångström are very difficult to identify even in the yellow-red spectral regions; this compromises any attempts to make signal-to-noise (S/N) estimates directly from the reduced spectra. After performing some numerical tests, we chose to use the photon counts of the final co-added one-dimensional spectral orders as primary S/N indicators. We made these calculations at $\lambda \simeq 6000$ Å, and they are listed in Table 3. The S/N values computed in this manner are in reasonable agreement with estimates that we made of point-to-point spectrum flux scatter in tiny spectral regions that appear to be free of line absorption. We also matched the observed spectra with synthetic spectra (see §6), and made S/N estimates from the scatter in the *observed minus computed* spectrum differences. These values also were in reasonable agreement with the primary photon-count statistics given in Table 3.

We measured the apparent RV shifts of our targets with the cross-correlation method provided in the *fxcor* (Fitzpatrick 1993) routine of IRAF. The cross-correlation technique requires a template spectrum. In order to avoid error contributions that can arise from rest-frame wavelength corrections made to a stellar standard-star spectrum, we opted against selecting the spectrum of another observed star as the template. Instead we created an artificial spectrum (see §6) with model atmospheric parameters similar to those of the NGC 752 programme stars. This spectrum was computed for the wavelength range from 5020 to 5990 Å. We then used the task *rvcorrect* given in IRAF's *rv* package to transform the geocentric into heliocentric RVs. We measured the RV for each star after combining individual exposures. However, we tested the RV scatter on individual exposures for a couple of stars, finding the scatter to be very small, $\sigma \simeq 0.05$ km s⁻¹.

Basic observational parameters of our programme stars along with measured RVs their associated errors from IRAF's *fxcor* task are listed in Table 3. In this table we

also give the RVs reported in Mer08, Car11 and Red12. From these data, for NGC 752 we obtain $\langle RV \rangle = 4.82 \pm 0.20$ km s⁻¹ ($\sigma = 0.63$ km s⁻¹), which is in good agreement with 5.04 ± 0.08 km s⁻¹ derived by Mer08.

The RVs of NGC 752 RG members as determined by Mer08 and confirmed in this study are not shared by the suggested non-members. For MMU 39, we derived $RV = -21.0$ km s⁻¹, about 26 km s⁻¹ away from the cluster mean, clearly ruling out membership. For MMU 215, our $RV = 9.5$ km s⁻¹ differs only by 4.7 km s⁻¹ from the cluster mean, but this still represents a 7σ deviation. Thus stars MMU 39 and MMU 215 do not belong to NGC 752 by this criterion. Nevertheless, we kept them in our sample to see if their chemical compositions would provide further information to address the question of cluster membership.

4 LINE LISTS AND EQUIVALENT WIDTHS

An important task in any spectroscopic abundance analysis is to create a list of relatively unblended lines that have reliable transition probabilities. This is especially important among stars that are cooler than G spectral type, because their spectra are composed of overlapping atomic and molecular transitions, which adversely affect many potentially useful lines.

4.1 Assembling the atomic and molecular line lists

The atmospheric parameter and chemical composition derivations in this work were conducted with the current version of the local thermodynamic equilibrium (LTE) line analysis and synthetic spectrum code MOOG⁷ (Sneden 1973). Here we discuss the input atomic/molecular line data.

⁷ <http://www.as.utexas.edu/~chris/moog.html>

The transitions employed in this study fell into three categories. (1) Unblended Ti and Fe neutral and ionized species lines that were used for model atmospheric parameter determinations. Abundances from these lines were calculated from their measured equivalent widths (*EW*). (2) Selected additional unblended atomic species lines that were used for relative abundance ratio determinations. Again, *EW*s were used to calculate their abundances. (3) Other atomic and molecular species lines that are heavily blended, or have significant hyperfine/isotopic substructure, were analyzed using spectral synthesis techniques.

Several sources were used to identify unblended lines: solar spectrum atlases (Delbouille et al. 1973, Kurucz et al. 1984, Wallace et al. 2011), solar spectrum identifications (Moore et al. 1966), the Arcturus spectrum atlas (Hinkle & Wallace 2005), and the interactive database of high-resolution standard star spectra SpectroWeb (Lobel 2011)⁸. Since it becomes increasingly difficult to determine the continuum in bluer spectral regions, we did not include the lines at wavelengths shorter than 4500 Å. We also tried to bypass the regions for which we applied telluric line removal. As a result, the overall spectral region we used for *EW* measurements ranges from 4500 Å to 7250 Å. Additionally, we discarded absorption lines with noticeable asymmetrical structure, even if we could not find any information about line contamination from the solar and Arcturus spectral resources.

As mentioned above, model atmospheric parameters were determined using transitions of Fe I, Fe II, Ti I, and Ti II. For these species, we imposed additional line strength limits, based on *EW* measurements and initial analyses of programme star MMU 77. Very strong lines in MMU 77, those with *EW*s higher than 150 mÅ (reduced widths $RW = \log(EW/\lambda) > -4.6$ at $\lambda \simeq 6000$ Å), and very weak lines ($EW < 10$ mÅ or $RW < -5.8$), were discarded from the list for all stars. Our final count of lines used for model parameter determinations includes 62 Fe I, 12 Fe II, 12 Ti I, and 5 Ti II lines. These line strength cutoffs were not applied to species with only a few available transitions (e.g., Na I and La II). We used various references for transition probabilities. The line list for all species, ordered by atomic number and ionization state, is shown in Table 4 (full version available online), where we list the wavelengths, lower excitation energies, log *gfs*, and the references for the adopted transition probabilities and hyperfine/isotopic splitting. Whenever possible, we used a single laboratory-based homogeneous transition probability study for a species. In particular, for Ti I, Ti II, Ni I, La II, Nd II, and Eu II we used lab data obtained by the University of Wisconsin atomic physics group. Frustratingly, there are no recent and comprehensive lab studies for Fe I and Fe II, the most crucial elements in any spectroscopic study of stars. Therefore, we have taken their transition probabilities mostly from O’Brian et al. (1991), NIST⁹ and VALD (Kupka et al. 2000)¹⁰ (see online version of Table 4). For the other species that we analyzed using their measured *EW*s (Si I, Ca I, Cr I, and Cr II), transition

Table 4. Line list of species. The machine-readable version of the entire table is available in the online journal.

Species	Wave. (Å)	LEP (eV)	log <i>gf</i>	EW / syn	Ref.
Li I	6707.9	0	0.17	syn	Kurucz
CH	4310			syn	Mas14 ^a
CH	4325			syn	Mas14
C ₂	5160			syn	Bro14 ^b
C ₂	5630			syn	Bro14
CN	8000			syn	Sne14 ^c
O I	6300.31	0	-9.72	syn	Caf08 ^d
Na I	5682.64	2.101	-0.70	syn	NIST
Na I	6154.23	2.101	-1.56	syn	NIST
Na I	6160.75	2.103	-1.26	syn	NIST
Mg I	5528.41	4.343	-0.62	syn	Kurucz
Mg I	5711.08	4.343	-1.83	syn	Kurucz
Mg I	7811.11	5.941	-0.95	syn	Kurucz
Al I	6696.02	3.14	-1.35	syn	Kurucz
Al I	6696.18	4.018	-1.58	syn	Kurucz
Al I	6698.67	3.14	-1.64	syn	Kurucz
Al I	7835.30	4.018	-0.65	syn	Kurucz
Si I	5488.98	5.614	-1.90	EW	Lob11 ^e
Si I	5517.53	5.082	-2.61	EW	VALD
Si I	5665.55	4.92	-2.04	EW	NIST

^a Masseron et al. (2014)

^b Brooke et al. (2014)

^c Sneden et al. (2014)

^d Caffau et al. (2008)

^e Lobel (2011)

probabilities were taken from sources noted in Table 4. Up to 164 lines are potentially available for *EW* measurements.

Fe-group species V I, Co I and Sc II transitions have significant hyperfine substructure, and their transitions should not be treated as single lines. We still derived their abundances from *EW* measurement, but with the blended-line analysis option in the MOOG code. For our work, we adopted the hyperfine substructure wavelengths and relative *gfs* from the Kurucz (2011)¹¹ line compendium. These species also lack good recent laboratory data. Therefore, we determined empirical log *gf* values for these species from a reverse solar analysis. We started the reverse analysis of Sc II with a transition probability taken from Lawler & Dakin (1989), and the initial transition probabilities of V I and Co I were taken from the Kurucz database. For this task, we measured *EW*s from a very high-resolution solar flux spectrum (Kurucz et al. 1984), and forced the total *gf* values to reproduce the solar abundances recommended by Asplund et al. (2009) (see §5.2 for further discussion of our solar analysis).

The remaining species of interest (C, N, O, Li I, Na I, Mg I, Cr I, Sc I, Cu I, Zn I, Y II, La II, Nd II, Eu II) have complex transitions, caused by their own substructures and/or by blending with other absorbers. For these species, we derived the abundances by spectrum synthesis, using recent transition probabilities whenever possible. Special mention should be made here of the availability of new, very extensive and accurate laboratory data for molecules that ap-

⁸ <http://spectra.freeshell.org/spectroweb.html>

⁹ http://physics.nist.gov/PhysRefData/ASD/lines_form.html

¹⁰ <http://vald.inasan.ru/~vald3/php/vald.php>

¹¹ <http://kurucz.harvard.edu/linelists.html>

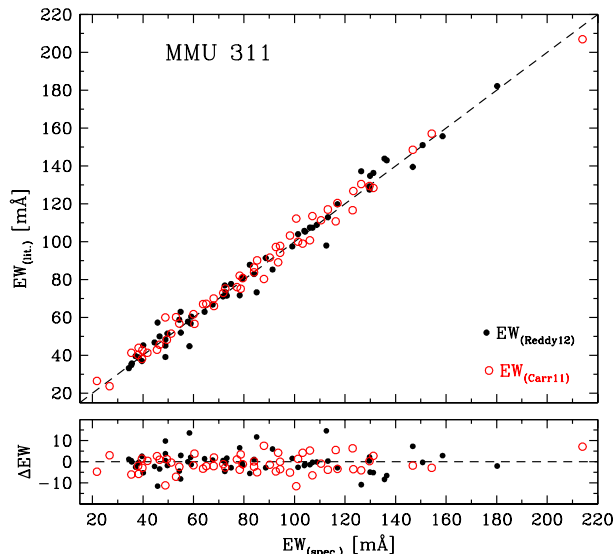


Figure 2. Comparison of our EWs with the ones given by Red12 and Car11 for MMU 311 (top panel). Differences in EWs are defined as $\Delta EW = EW_{literature} - EW_{this\ study}$ (bottom panel).

pear in almost every spectral region of RG stars: the $^{12}\text{C}_2$ and $^{12}\text{C}^{13}\text{C}$ Swan system (Brooke et al. 2013; Ram et al. 2014), the ^{12}CH and ^{13}CH (Masseron et al. 2014) G-band, ^{12}CN and ^{13}CN (Brooke et al. 2014; Sneden et al. 2014), red and blue systems, and MgH (Hinkle et al. 2013). With the new gf line data for these molecules, the accuracy of C and N abundance determinations can be significantly improved. Furthermore, syntheses of various atomic transitions that are surrounded by these molecular lines can now be accomplished with greater confidence.

4.2 Equivalent width measurements

We measured EW s in a semi-automated manner, using a modified version of the Interactive Data Language (IDL) code that was introduced by Roederer et al. (2010) and refined by Brugamyer et al. (2011). The observed line profiles were matched interactively with theoretical Gaussian line profiles in most cases, or Voigt profiles for some of the stronger lines. Central line depths were also recorded for use in estimating initial values of effective temperature (T_{eff}) for the programme stars via the line depth ratio method discussed below. In Table 5 (also available online) we have listed EW s measurements of all our target stars.

We tested the accuracy of our EW s measurements in several ways. First, we re-measured the EW s of some lines using the Gaussian fit approximation in IRAF’s *splot* task; good agreement was found with our IDL code results. Second, we compared our EW s with those measured by Car11 and Red12. In Figure 2 we show EW correlations for MMU 311, the NGC 752 RG shared by all three studies. For 54 lines used by us and Red12, we find $\Delta EW_{Red12} = 0.58 \pm 0.63 \text{ m}\text{\AA}$ ($\sigma = 4.69 \text{ m}\text{\AA}$), and for 59 lines shared with Car11 we find $\Delta EW_{Car11} = 0.60 \pm 0.60 \text{ m}\text{\AA}$ ($\sigma = 4.64 \text{ m}\text{\AA}$). Considering the differences in spectroscopic data and measurement methods among these three studies, we regard the EW agreement as satisfactory.

5 MODEL ATMOSPHERIC PARAMETERS

5.1 Methods

We determined parameters for the programme stars with a standard approach of calculating abundances from the EW s of Fe and Ti neutral and ionized lines, and requiring of these abundances:

- (i) for T_{eff} , that there be no difference, on average, in the Fe I abundances of low and high excitation (χ) potential lines;
- (ii) for ξ_t , that there be no difference on average between Fe I and Ti I abundances of weak and strong lines (no apparent trend with reduced width, $RW = \log(EW/\lambda)$);
- (iii) for $\log g$, that the mean abundances of neutral and ionized Fe and Ti lines agree;
- (iv) for $[\text{Fe}/\text{H}]$, that the value employed in creating the model atmosphere agrees with the derived value.

These four atmospheric parameters are somewhat coupled, e.g., the lowest excitation lines are often the strongest ones. Since we have a larger excitation potential range for Ti I than the other species, and more Fe I than the other species, and more Fe I and Fe II lines than Ti I and Ti II lines, we gave extra weight to Fe in deriving model atmosphere parameters. After several trials we adopted a uniform 0.35 weight for Ti lines. The parameter results proved to be insensitive to the exact weight that was employed here.

We were mindful of the potential for undesired correlations among the atmospheric parameters as discussed by Torres et al. (2012). Therefore, we used a semi-automated iterative approach in model derivation, one that allowed examination of abundance changes caused by each alteration in T_{eff} , ξ_t , $\log g$, and metallicity values. To accomplish the iterations more efficiently, we used a code that altered the input model parameters in response to abundance slopes with χ and RW , and mismatches between neutral and ionized species or input and output metallicities. This code is a modified version of one that has been employed in previous large-sample abundance analyses by Hollek et al. (2011) and Roederer et al. (2014). The abundance trends in text and graphical form are available for inspection in each iteration, so that user judgment can be applied to parameter changes attempted by the code. Implementation of this scheme is discussed in §5.3.

5.2 Initial parameters

Gray & Johanson (1991) demonstrated that precise T_{eff} values for F–K dwarf stars could be obtained from calibrations of the central depth ratios of absorption line pairs selected to have different responses to changes in temperature. Their basic line depth ratio (LDR) method was expanded in T_{eff} , $\log g$, and metallicity space in subsequent studies (e.g., Strassmeier & Schordan 2000, Gray & Brown 2001). In Afşar et al. (2012) we employed several LDRs to confirm the T_{eff} values derived from Fe I excitation equilibria for a sample of red horizontal-branch stars.

A comprehensive examination and re-evaluation of the LDR technique was done by Biazzo et al. (2007a,b). Those authors identified 15 pairs formed from 28 total lines in the 6199–6274 Å spectral range whose depth ratios are sensitive functions of T_{eff} , but relatively insensitive to $\log g$ and

Table 5. Equivalent width measurements (in mÅ) of the NGC 752 RG members. The machine-readable version of the entire table is available in the online journal.

Species	Wavelength (Å)	MMU									
		1	3	11	24	27	77	137	295	311	1367
Si I	5488.98	32.4	31.7	33.3	34.7	35.6	32.3	34.3	34.6	35.6	35.5
Si I	5517.53	22.7	21.9	22.6	22.7	24.5	23.7	26.4	29.2	28.4	29.7
Si I	5665.55	61.4	59.9	62.1	26.9	64.9	64.8	66.7	61.1	67.6	67.1
Si I	5701.10								57.4	54.4	
Si I	5793.07	58.0	52.2	59.8	59.9	61.5	58.7	62.2	62.7	63.8	61.2

Table 6. Photometric and spectroscopic atmospheric parameters.

Star	$T_{\text{eff},(B-V)}$ (K)	$T_{\text{eff},(V-K)}$ (K)	$T_{\text{eff},(LDR)}$ (K)	$\log g_{\text{phot}}$ (cm s^{-2})	$T_{\text{eff},\text{spec}}$ (K)	$\log g_{\text{spec}}$ (cm s^{-2})	ξ_{spec} (km s^{-1})	[M/H]
Cluster Members								
MMU 1	4979	4888	5038 ± 18	2.81	5005	2.95	1.07	-0.07
MMU 3	4891	4788	4977 ± 21	2.79	4886	2.76	1.10	-0.10
MMU 11	4954	4910	5056 ± 29	2.74	4988	2.80	1.14	-0.06
MMU 24	4860	4810	4991 ± 22	2.54	4839	2.42	1.23	-0.09
MMU 27	4862	4798	4991 ± 26	2.64	4966	2.73	1.16	-0.04
MMU 77	4824	4709	4906 ± 21	2.67	4874	2.80	1.15	-0.05
MMU 137	4830	4771	4985 ± 19	2.60	4832	2.51	1.29	-0.16
MMU 295	4960	4892	5062 ± 29	2.74	5039	2.88	1.10	-0.05
MMU 311	4810	4747	4950 ± 20	2.63	4874	2.68	1.24	-0.02
MMU 1367	4844	4801	4990 ± 32	2.52	4831	2.42	1.22	-0.07
Non Members								
MMU 39			5050 ± 39		4811	2.20	1.22	-0.33
MMU 215			4671 ± 61		4350	1.81	1.29	+0.09

[Fe/H], at least for the metallicities of typical disk stars. Biazzo et al. (2007a) developed cubic polynomials to express T_{eff} as a function of a depth ratio for each line pair, both for sharp-lined stars and ones with significant rotational broadening. As discussed in §4.2 we measured as many LDR lines (Table 1 of Biazzo et al.) as possible for each programme star. We missed only two lines from the Biazzo et al. list, as they fell in one of our echelle spectrum inter-order data gaps. Then we applied the polynomial coefficients for non-rotationally-broadened stars (their Table 2) to estimate individual LDR temperatures. A straight mean of 14 LDRs from 26 lines yielded our final $T_{\text{eff}}(\text{LDR})$ estimates. These values are tabulated in Table 6, along with their standard deviations and the number of participating LDR pairs.

We also estimated photometric effective temperatures of our programme stars from the B , V , and K magnitudes in Table 2. For this purpose we used metallicity-dependent T_{eff} versus color calibrations for giant stars given by Ramírez & Meléndez (2005). The temperatures that we calculated for $(B - V)_0$ and $(V - K)_0$ ¹² colors are given in Table 6. Metallicity is an important consideration in color-temperature calibrations, affecting $(B - V)$ more than $(V - K)$ because the B band suffers a large amount of line blanketing. Therefore, since $(V - K)_0$ colors are nearly metallicity independent, for the initial $T_{\text{eff}}(\text{phot})$ we only used the computed $(V - K)_0$ temperature. We then calculated a non-weighted mean of $T_{\text{eff}}(\text{phot})$ and $T_{\text{eff}}(\text{LDR})$ to

form the initial T_{eff} estimate for the programme stars; these also are given in Table 6.

To calculate physical (cluster) gravities we used the standard equation,

$$\log g_{\star} = 0.4 (M_{V\star} + BC - M_{\text{Bol}(\odot)}) + \log g_{\odot} + 4 \log\left(\frac{T_{\text{eff}\star}}{T_{\text{eff}\odot}}\right) + \log\left(\frac{m_{\star}}{m_{\odot}}\right). \quad (1)$$

The adopted solar parameters were $M_{\text{bol}} = 4.75$, $\log g = 4.44$ and $T_{\text{eff}} = 5780$ K. Temperature-dependent bolometric corrections were calculated with the polynomial formula and coefficients given in Table 1 of Torres (2010). For NGC 752, the absolute magnitudes M_V were computed with the V magnitudes of Table 2, and the cluster distance modulus, reddening and turnoff mass were used as given in Table 1.

To calculate the physical gravities we varied the stellar masses from 1.5 to 1.95 M_{\odot} , which is a range from the minimum turnoff mass suggested in the literature to RG mass provided by the PARSEC isochrone we applied. The results of these experiments always led us to the spectroscopic gravities that were expected for the RG stars and they always remained in our uncertainty limits (see §5.4). Therefore, for masses of target stars we adopted 1.5 M_{\odot} , which is the turnoff mass of NGC 752 suggested in Bartašiūtė et al. (2007). Previous studies (§2) suggest about solar metallicity for NGC 752, so we used an initial value of [M/H] = 0. Finally, we adopted a microturbulent velocity that is typical for solar-metallicity RG stars: $\xi = 1.2 \text{ km s}^{-1}$.

¹² The K magnitude is from 2MASS, and Ramírez & Meléndez (2005) label the color $(V - K_2)$.

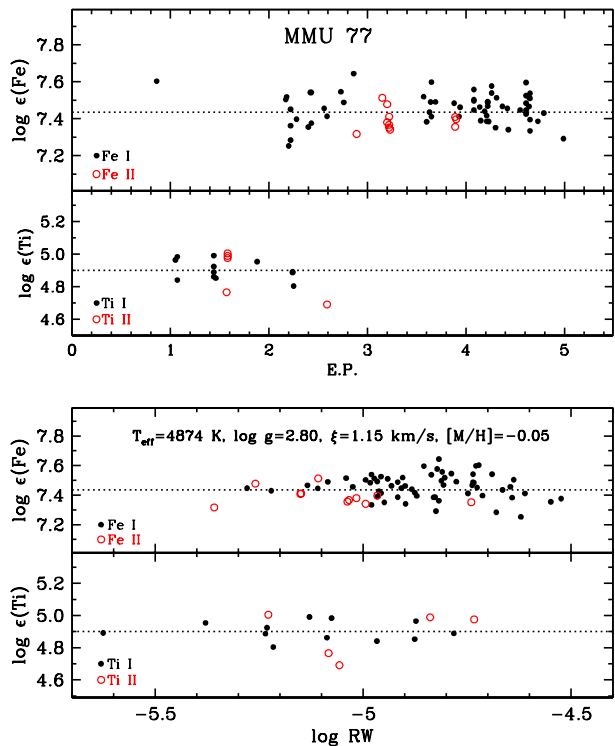


Figure 3. An example model atmosphere determination using both ionized and neutral species of Fe and Ti for MMU 77.

5.3 Final parameters

We fed the Ti and Fe *EWs* (§4.2), trial model atmospheres, a set of instructions (e.g., model parameter goodness of fit criteria), and needed data (e.g., cluster distance modulus, magnitudes and colors of individual stars) to the semi-automated model iteration code. New grids of ATLAS9 Model Atmospheres from Castelli & Kurucz (2003) were used to compute the stellar atmosphere models with opacity distribution functions and no convective overshooting. These grids were interpolated to the desired values of T_{eff} , $\log g$, and $[M/H]$ with software developed by Andy McWilliam and Inese Ivans, kindly made available for our use.

After establishing initial model atmosphere parameters, we conducted the final parameter search with the code and the model convergence criteria described in §5.1. In Figure 3 we plot line-by-line abundance results for star MMU 77 after completion of model iterations. We will be using MMU 77 in this and several more illustrative plots, because this star has model atmospheric parameters that are very similar to all others in our sample. In this figure we have correlated the MMU 77 line abundances with their *EP* and *RW* values; there is no apparent trend between the abundances and these two parameters.

The initial and final model atmosphere parameters for all of our targets are given in Table 6. We also summarize in Table 7 the atmospheric parameters of our programme stars that were obtained by Gil89, Car11, and Red12.

Comparisons of the final iterated effective temperatures from our spectra, $T_{\text{eff}}(\text{spec})$, and the initial T_{eff} estimates from photometry and LDR measurements are shown in Figure 4. On average, values are in reasonable accord, with the mean difference being $\langle T_{\text{eff}}(\text{initial}) - T_{\text{eff}}(\text{final}) \rangle = -18$ K.

However, offsets can be seen among the individual T_{eff} determination methods. For both photometric temperatures, uncertainties arise from reddening and distance parameters, and the overall offsets can come from the color- T_{eff} calibrations. We derive $\langle T_{\text{eff}}(B-V) - T_{\text{eff}}(\text{spec}) \rangle = -32 \pm 13$ and $\langle T_{\text{eff}}(V-K) - T_{\text{eff}}(\text{spec}) \rangle = -102 \pm 16$. For temperatures calculated with LDR method, we find $\langle T_{\text{eff}}(\text{LDR}) - T_{\text{eff}}(\text{spec}) \rangle = 81 \pm 18$. Continuum placement uncertainties can be of concern here, so we made numerical experiments in which the continuum choices were changed to substantially lower and higher values. These resulted in $T_{\text{eff}}(\text{LDR})$ changes $\ll 25$ K because the LDR method compares depths of lines situated very close in wavelength, a feature central to the original LDR method design (Gray & Johanson 1991). In Figure 4, one can see that the three coolest stars are offset in the comparisons by ~ 50 – 70 K compared to the other seven stars. This small offset does not substantially effect metallicities and relative abundance ratios of these stars with respect to the majority of our sample.

A comparison of calculated gravities ($\log g_{\text{phot}}$) with spectroscopic gravities ($\log g_{\text{spec}}$) is given in Figure 5. They agree well with each other: $\langle \Delta \log g \rangle = -0.03 \pm 0.03$. There is a small trend that is mostly due to the three coolest, lowest gravity RGs in our sample. Differences in the evolutionary status of the members (see §7) may create such a fluctuation.

The metallicities we derived for the NGC 752 RGs from the model atmosphere analysis have a slight scatter around the solar metallicity (Table 6). The mean metallicity of the cluster calculated from these 10 members is $\langle [M/H] \rangle = -0.07 \pm 0.04$. The metallicities of all NGC 752 targets are in agreement except for MMU 137, which has a metallicity of $[M/H] = -0.16$. However, this star also has one of the lowest $\log g$ values in our sample.

We also applied these atmospheric parameter determination methods to the suspected non-member stars MMU 39 and MMU 215. Since no parallax, reddening, and mass data are available for these stars, we could not calculate their $T_{\text{eff}}(B-V)$, $T_{\text{eff}}(V-K)$ and $\log g_{\text{phot}}$ values. Therefore we used the LDR temperatures for T_{eff} and adopted typical RG $\log g$ values for the initial parameter guesses. We found $[M/H] = -0.33$ for MMU 39 ($\sim 8\sigma$ from the cluster mean), and $[M/H] = +0.09$ ($\sim 3\sigma$ from the mean) for MMU 215. Clearly NGC 752 membership is ruled out for these two stars from our *RV* and metallicity computations, in agreement with the results of Mer08. These stars are eliminated from further discussion in this paper.

5.4 Parameter uncertainties

We estimated the internal uncertainties in atmospheric parameters by running a series of analyses on the spectral data of MMU 77. First we changed the effective temperature in 50 K steps while keeping the other atmospheric parameters fixed. This process was repeated until the magnitude of the difference between high and low excitation potential Fe I lines exceeded the σ value of the initial line abundances. This method led to an average T_{eff} uncertainty of ~ 100 K. We applied a similar method to estimate the internal uncertainty for microturbulence velocity. This time we only changed the velocity in 0.1 km s^{-1} steps and focused on the abundance changes in the elements that have both neutral and ionized lines: Ti I, Ti II, Fe I, Fe II, Cr I, and Cr II. The

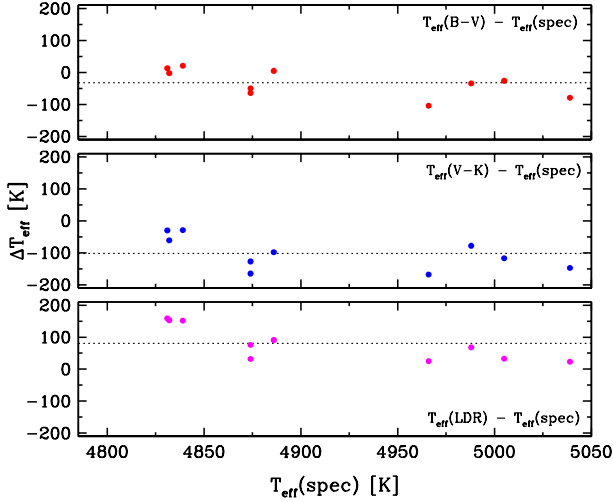


Figure 4. Comparison of $\Delta T_{\text{eff}} = T_{\text{eff}}(x) - T_{\text{eff}}(\text{spec})$ with spectroscopic T_{eff} . $T_{\text{eff}}(x)$ stands for the temperatures of $T_{\text{eff}}(B - V)$, $T_{\text{eff}}(V - K)$ and $T_{\text{eff}}(\text{LDR})$.

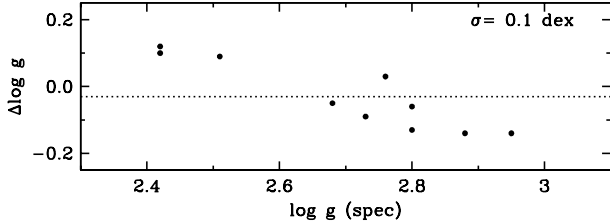


Figure 5. Comparison of $\Delta \log g = \log g_{(\text{phot})} - \log g_{(\text{spec})}$ with derived spectroscopic $\log g$.

typical average uncertainty achieved for ξ_t was 0.3 km s^{-1} . The internal uncertainty level for $\log g$ was also derived by taking into account the abundance differences in both neutral and ionized species. The highest abundance difference (over $\pm 1\sigma$ level) between Cr I and Cr II was found to be 0.06 dex, which corresponds to an uncertainty of 0.16 dex in $\log g$.

To estimate the external uncertainty in our T_{eff} values, we compared them with the available T_{eff} estimates for

Table 7. Spectroscopic atmospheric parameters of NGC 752 members studied by Gil89, Car11 and Red12.

Star	$T_{\text{eff}, \text{spec}}$ (K)	$\log g_{\text{spec}}$ (cm s^{-2})	ξ_{spec} (km s^{-1})	$[M/H]$
		Gil89		
MMU 1	5000	2.85	1.90	0.10
MMU 77	4900	2.85	1.80	0.20
MMU 295	5000	2.90	1.80	0.20
MMU 311	4900	2.85	1.90	0.10
		Car11		
MMU 1	5050	3.10	1.30	0.045
MMU 311	4800	3.20	1.20	0.16
		Red12		
MMU 77	4850	2.65	1.26	-0.03
MMU 137	4850	2.50	1.36	-0.01
MMU 295	5050	2.85	1.47	-0.045
MMU 311	4850	2.60	1.45	-0.04

these stars that were also investigated by Gil89, Car11, and Red12.: Gil89, Car11 and Red12. The atmospheric parameters obtained in these studies are also listed in Table 7. We also calculated the photometric and LDR temperatures and investigated the differences between these two temperatures and our spectroscopically derived T_{eff} values (Figure 4). An overall comparison of the differences among these temperatures yielded an average external uncertainty of about 150 K.

The external uncertainty in $\log g$ was estimated by comparing our $\log g$ values with the ones gathered from the literature for shared NGC 752 stars. We have made use of the same set of studies that were used to estimate the uncertainty in T_{eff} . Our results are usually in good agreement with the published ones, with an average scatter of ~ 0.2 dex. For one star, MMU 311, Car11 reported a $\log g$ value of 3.2. Since this result is significantly different from the average provided by other studies, we did not include it in our uncertainty estimations. In Figure 5, we plot the spectroscopic $\log g$ versus calculated $\log g$ values. The standard deviation of the differences between these two $\log g$ values was found to be ~ 0.1 dex.

Taking into account both internal and external uncertainty levels, the typical errors we adopted are ± 150 K in T_{eff} , ± 0.25 dex in $\log g$ and $\pm 0.3 \text{ km s}^{-1}$ in ξ_t . We also investigated the uncertainties in elemental abundances caused by these adopted uncertainties, and have listed them in Table 8. The sensitivity of $[X/\text{Fe}]$ to the uncertainties in model atmosphere parameters is typically much smaller than the values of Table 8 because of correlations in the ionization balances of most species of interest here.

We also investigated the uncertainty limits for $^{12}\text{C}/^{13}\text{C}$ ratios. Adopting different model atmospheres was not very effective in changing the isotopic ratios since the ^{12}CN and ^{13}CN molecular lines are essentially the same in excitation energies, thus not really sensitive to the changes in model atmosphere parameters. To determine the uncertainties, we fit synthetic spectra with varying $^{12}\text{C}/^{13}\text{C}$ ratios to the observed ^{12}CN and ^{13}CN features. The resulting uncertainty limits we derived using this method are listed in Table 8.

6 ABUNDANCE ANALYSIS

Abundances of species with non-blended transitions that could be treated as single absorbers were derived from their EW measurements. Other species exhibiting complex hyperfine splitting and/or isotope shifts, and those with lines that suffer significant blending of lines by other species, were treated either to blended-line analyses or full synthetic-observed spectrum matching. Several figures in this section will illustrate the comparisons of different synthetic spectra with observed data points.

To normalize our abundances, we re-measured all of our stellar lines in the integrated solar flux atlas of Kurucz et al. (1984). The solar model atmosphere was calculated using the Castelli & Kurucz (2003) grid, assuming $T_{\text{eff}} = 5777$ K, $\log g = 4.44 \text{ cgs}$, $\xi = 0.85 \text{ km}^{-1}$. Abundances found from this analysis are listed in Table 9 alongside the solar abundances recommended by Asplund et al. (2009). Since we assumed solar abundances given by Asplund et al. for

Table 8. Sensitivity (σ) of derived abundances to the model atmosphere changes within uncertainty limits for the star MMU 77.

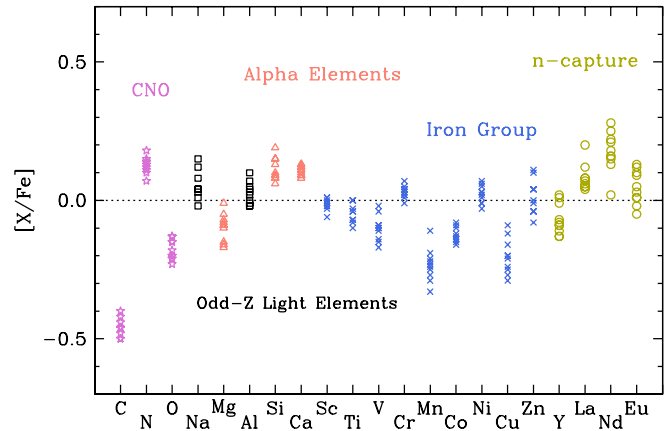
Species	$\Delta T_{\text{eff}}(\text{K})$ -150 / +150	$\Delta \log g$ -0.25 / +0.25	$\Delta \xi_t (\text{kms}^{-1})$ -0.3 / +0.3
Li I	-0.14 / +0.26	+0.06 / +0.09	+0.09 / +0.11
C	+0.08 / +0.11	+0.08 / +0.09	+0.09 / -0.01
N	-0.05 / +0.10	0.00 / +0.05	+0.03 / +0.01
O	-0.01 / +0.09	-0.01 / +0.19	-0.01 / +0.09
Na I	-0.14 / +0.07	-0.01 / -0.04	+0.15 / -0.06
Mg I	-0.08 / +0.05	0.00 / -0.03	+0.03 / -0.07
Al I	-0.15 / 0.00	-0.10 / -0.07	0.00 / -0.10
Si I	+0.08 / -0.03	-0.04 / +0.05	+0.04 / -0.04
Ca I	-0.13 / +0.14	+0.04 / -0.04	+0.15 / -0.16
V I	-0.24 / +0.23	0.00 / 0.00	+0.05 / -0.05
Cr I	-0.15 / +0.16	+0.02 / 0.00	+0.09 / -0.09
Cr II	+0.13 / -0.08	-0.10 / +0.12	+0.13 / -0.11
Sc II	+0.06 / 0.00	-0.08 / +0.13	+0.11 / -0.10
Ti I	-0.21 / +0.19	0.00 / 0.00	+0.08 / -0.06
Ti II	+0.07 / 0.00	-0.09 / +0.13	+0.12 / -0.11
Mn I	-0.22 / +0.13	-0.09 / -0.02	+0.05 / -0.12
Fe I	-0.05 / +0.10	0.00 / +0.02	+0.15 / -0.14
Fe II	+0.19 / -0.10	-0.12 / +0.15	+0.09 / -0.09
Co I	-0.05 / +0.12	-0.02 / +0.07	+0.02 / -0.02
Ni I	-0.03 / +0.10	-0.03 / +0.06	+0.16 / -0.15
Cu I	-0.04 / +0.13	0.00 / +0.08	+0.13 / -0.09
Zn I	-0.04 / -0.07	-0.09 / +0.01	0.00 / -0.14
Y II	-0.17 / -0.07	-0.12 / -0.07	+0.06 / -0.24
La II	-0.05 / +0.01	-0.11 / +0.04	0.00 / -0.04
Nd II	-0.04 / -0.02	-0.15 / +0.07	+0.07 / -0.12
Eu II	-0.04 / 0.00	-0.09 / +0.01	+0.01 / -0.05
$^{12}\text{C}/^{13}\text{C}$	2 / 0	5 / -3	-1 / 0

Sc II, V I, and Co I, no independent solar abundance was derived for these elements. Estimated sigmas given in parenthesis were determined by taking into account the continuum placement, goodness of the fit and smoothing of the synthetic spectrum. For most species, Of course, we employ standard LTE analyses, while more detailed physics (e.g., accounting for solar granulation, multi-stream atmospheric models, non-LTE corrections) of Asplund et al. is being neglected. Even so, our results are mostly in agreement with those of Asplund et al.. Our $[X/H]$ and $[X/Fe]$ results for NGC 752 will be quoted differentially with respect to our own solar analysis abundances.

We derived abundances for 26 species of 23 elements. We will organize the discussion of these abundances by element groups: α (Mg, Si, Ca); light odd-Z (Na, Al); Fe-group (Sc, Ti, V, Cr, Mn, Fe, Co, Ni, Cu, Zn); n -capture (Y, La, Nd, Eu); and p -capture (Li, C, N, O). In Table 10 (also available online¹³), we list the derived abundances for individual RG members of NGC 752 and the mean abundances for the cluster, $\langle [X/Fe] \rangle$. The mean abundances from Red12 and Car11 are also given in the last two columns of the table for comparison. The general distribution of solar normalized elemental abundances can be seen in Figure 6. The mean abundances of most species (20 out of 26) fluctuate within ± 0.15 dex of their solar values. Abundances of C, Mn, Cu,

Table 9. Solar abundances.

Species	$\log \epsilon_{\odot}$ (this study)	$\log \epsilon_{\odot}$ (Asplund et al. 2009)
Li I	1.05 \pm (0.05)	1.05 \pm 0.10
C	8.43 \pm (0.05)	8.43 \pm 0.05
N	8.13 \pm (0.05)	7.83 \pm 0.05
O	8.69 \pm (0.05)	8.69 \pm 0.05
Na I	6.34 \pm (0.10)	6.24 \pm 0.04
Mg I	7.63 \pm 0.16	7.6 \pm 0.04
Al I	6.33 \pm 0.18	6.45 \pm 0.03
Si I	7.57 \pm 0.05	7.51 \pm 0.03
Ca I	6.31 \pm 0.03	6.34 \pm 0.04
Sc II		3.15 \pm 0.04
Ti I	4.88 \pm 0.06	4.95 \pm 0.05
Ti II	4.98 \pm 0.05	
V I		3.93 \pm 0.08
Cr I	5.61 \pm 0.04	5.64 \pm 0.04
Cr II	5.72 \pm 0.08	
Mn I	5.41 \pm 0.06	5.43 \pm 0.04
Fe I	7.42 \pm 0.04	7.50 \pm 0.04
Fe II	7.45 \pm 0.04	
Co I		4.99 \pm 0.07
Ni I	6.24 \pm 0.07	6.22 \pm 0.04
Cu I	4.07 \pm 0.10	4.19 \pm 0.04
Zn I	4.51 \pm (0.05)	4.56 \pm 0.05
Y II	2.19 \pm 0.04	2.21 \pm 0.05
La II	1.15 \pm 0.06	1.10 \pm 0.04
Nd II	1.37 \pm (0.05)	1.42 \pm 0.04
Eu II	0.54 \pm 0.08	0.52 \pm 0.04


Figure 6. $[X/Fe]$ values of the species studied for the entire RG sample. Dotted line represents the solar values. Abundances of CNO, odd-Z, alpha, iron-group and n -capture elements are shown by stars, squares, triangles, crosses and empty circles, respectively.

and Nd depart from the solar abundance mix by ≥ 0.2 dex. We will discuss these and other elemental abundance results in the following subsections.

6.1 α , Odd-Z, Fe-group and Neutron-capture elements

α and Odd-Z elements: The analyzed α elements are Mg, Si, and Ca. We did not include Ti because even though Ti has been labeled as an α element in metal poor stars, its dominant isotope $^{48}\text{Ti}_{22}$ is not an even multiple of α parti-

¹³ Online version of this table will also include the number of lines used for the species and the scatter of the abundance obtained from each species.

Table 10. Elemental abundances of individual stars and average abundances ($\langle[X/Fe]\rangle$) for NGC 752. The average abundances from Red12 and Car11 are also given. The machine-readable version of the entire table is available in the online journal.

Species	MMU										$\langle[X/Fe]\rangle$	Red12	Car11
	1	3	11	24	27	77	137	295	311	1367			
[C/Fe]	-0.48	-0.50	-0.42	-0.46	-0.46	-0.46	-0.40	-0.44	-0.50	-0.46	-0.46 ± 0.03
[N/Fe]	0.15	0.07	0.10	0.14	0.18	0.12	0.14	0.14	0.13	0.11	0.13 ± 0.03
[O/Fe]	-0.21	-0.23	-0.21	-0.20	-0.13	-0.13	-0.15	-0.15	-0.18	-0.20	-0.18 ± 0.04	...	0.03
[Na I/Fe]	0.04	-0.02	0.04	0.12	0.04	0.01	0.15	0.03	0.04	0.08	0.05 ± 0.05	0.12	0.01
[Mg I/Fe]	-0.15	-0.08	-0.10	-0.01	-0.07	-0.09	-0.05	-0.17	-0.16	-0.09	-0.09 ± 0.05	-0.01	0.12
[Al I/Fe]	-0.02	0.02	-0.02	0.07	0.03	0.05	0.10	-0.01	0.00	0.04	0.03 ± 0.04	0.15	-0.12
[Si I/Fe]	0.06	0.08	0.08	0.15	0.09	0.13	0.19	0.09	0.10	0.15	0.11 ± 0.04	0.11	0.02
[Ca I/Fe]	0.10	0.12	0.08	0.13	0.11	0.13	0.11	0.09	0.09	0.12	0.11 ± 0.02	0.03	-0.09
[Sc II/Fe]	0.00	-0.03	-0.01	-0.02	0.01	0.01	-0.01	-0.02	-0.01	-0.06	-0.01 ± 0.02	0.04	0.03
[Ti I/Fe]	-0.03	-0.06	-0.08	-0.08	0.04	0.03	-0.04	0.00	-0.04	-0.09	-0.03 ± 0.05	-0.07	-0.03^a
[Ti II/Fe]	0.02	-0.03	-0.01	-0.09	-0.05	-0.10	-0.11	0.00	-0.10	-0.11	-0.05 ± 0.05	-0.04	...
[V I/Fe]	-0.09	-0.11	-0.15	-0.14	-0.04	-0.02	-0.10	-0.09	-0.10	-0.17	-0.10 ± 0.05	0.03	0.01
[Cr I/Fe]	0.04	0.05	-0.01	0.05	0.08	0.04	0.07	-0.02	-0.04	0.02	0.03 ± 0.04	-0.03	0.00
[Cr II/Fe]	0.01	0.03	0.02	0.09	0.00	0.05	0.02	0.08	0.02	0.01	0.03 ± 0.03	0.02	...
[Mn I/Fe]	-0.21	-0.29	-0.23	-0.19	-0.24	-0.22	-0.25	-0.33	-0.27	-0.11	-0.23 ± 0.06	-0.13	...
[Fe I/H]	0.04	-0.05	0.03	-0.05	0.08	0.04	-0.08	0.07	0.07	-0.02	0.01 ± 0.06	-0.04	0.08^a
[Fe II/H]	-0.02	-0.07	-0.01	-0.11	-0.06	-0.06	-0.16	-0.01	0.01	-0.08	-0.06 ± 0.05	-0.02	...
[Co I/Fe]	-0.13	-0.15	-0.16	-0.14	-0.09	-0.08	-0.10	-0.14	-0.12	-0.14	-0.12 ± 0.03	-0.02	0.01
[Ni I/Fe]	0.01	-0.03	-0.01	0.02	0.07	0.06	0.03	0.05	0.03	-0.01	0.02 ± 0.03	-0.01	-0.01
[Cu I/Fe]	-0.12	-0.27	-0.20	-0.20	-0.16	-0.09	-0.21	-0.29	-0.25	-0.24	-0.20 ± 0.06	-0.11	...
[Zn I/Fe]	-0.08	0.00	-0.04	0.11	-0.01	0.04	0.10	-0.04	0.04	0.04	0.02 ± 0.06	-0.10	...
[Y II/Fe]	-0.09	-0.09	-0.01	0.01	-0.07	0.02	-0.13	-0.08	-0.11	-0.13	-0.06 ± 0.05	0.03	-0.03^a
[La II/Fe]	0.08	0.05	0.05	0.08	0.07	0.20	0.12	0.05	0.06	0.04	0.08 ± 0.05	0.13	0.18
[Nd II/Fe]	0.16	0.02	0.21	0.18	0.25	0.28	0.22	0.15	0.16	0.13	0.18 ± 0.07	0.06	0.34
[Eu II/Fe]	0.01	0.13	-0.05	0.10	0.01	0.12	0.09	-0.02	0.05	0.03	0.05 ± 0.06	0.07	...

^a Car11 list the average abundances of the same species, e.g. [Fe I/H] and [Fe II/H] abundances are given as an average: [Fe/H]. Here, we list the abundances from Car11 according to species with the majority of the analyzed lines.

cles. We therefore treat Ti as a Fe-peak. Si and Ca abundances were derived from *EW* measurements of their neutral species lines, while we applied synthetic spectra to determine the Mg abundances. Note that three Mg I lines were used, but the feature at 7811.1 Å has very large damping wings that cannot be modeled with standard line parameters; the line wings are far too broad. To compensate, we arbitrarily increased the damping constants for this line based on matching it to the solar spectrum. We also analyzed the 5170 Å region that encompasses two of the very saturated Mg I “b” lines, but we did not include their derived abundances in the mean Mg abundance. We employed spectrum syntheses to determine the abundances of odd-*Z* light elements of interest, Na and Al.

The overall comparison of the average abundances of all species with recent NGC 752 high-resolution abundance studies by Red12 and Car11 is given in Table 10. Here and throughout the rest of the paper, our definition of comparison is the difference between the mean cluster abundances from these studies and our results: for Red12, $\Delta[X/Fe]_R \equiv [X/Fe]_{\text{Red12}} - [X/Fe]_{\text{this study}}$, and for Car11, $\Delta[X/Fe]_C \equiv [X/Fe]_{\text{Car11}} - [X/Fe]_{\text{this study}}$. In Red12, the mean abundances were determined from four cluster members. Car11 also derived the abundances of four members, but two of them have been reported as spectroscopic binaries by Mer08. Our results are mostly in good agreement with Red12 within error limits: $\Delta[\text{Mg}/\text{Fe}]_R = 0.06$, $\Delta[\text{Ca}/\text{Fe}]_R = -0.08$. The discrepancies with Car11 are

larger: $\Delta[\text{Mg}/\text{Fe}]_C = 0.23$ and $\Delta[\text{Ca}/\text{Fe}]_C = -0.20$. Our Si I abundances agree well with those of Red12 but $\Delta[\text{Si}/\text{Fe}]_C = -0.09$. The differences between the abundances obtained from Na I lines in our study and the others are small, but for the Al I, the differences are $\Delta[\text{Al}/\text{Fe}]_R = 0.12$ and $\Delta[\text{Al}/\text{Fe}]_C = -0.15$. The reason for these discrepancies most likely stem from different analysis methods employed in these studies. For instance, while we used the spectral synthesis method to obtain Al I abundances, Red12 and Car11 used *EWs*.

Fe-group elements: The abundances of Ti I, Ti II, Cr I, Cr II and Ni I were determined from *EWs* in single-line analyses. As discussed in §4.1, several Fe-group species (Sc II, V I, Co I) have significant hyperfine substructure and no recent comprehensive transition probability studies. Therefore, we conducted reverse solar analyses to derive their transition probabilities. Hyperfine component parameters from the Kurucz database were adopted for these transitions. We applied blended-line *EW* analyses (see §4.1) to determine the “solar” *gf*’s, and then used these to calculate the abundances.

We employed full synthetic spectrum computations for other Fe-group elements in our list: Mn I, Cu I, and Zn I. We used three absorption lines of Mn I located near ~ 6016 Å for Mn abundance determination. These transitions have hyperfine structure and the region is also contaminated by CN absorption. We also used three lines of Cu I to obtain its abundance. Although the Cu I line at 5782.1 Å is near

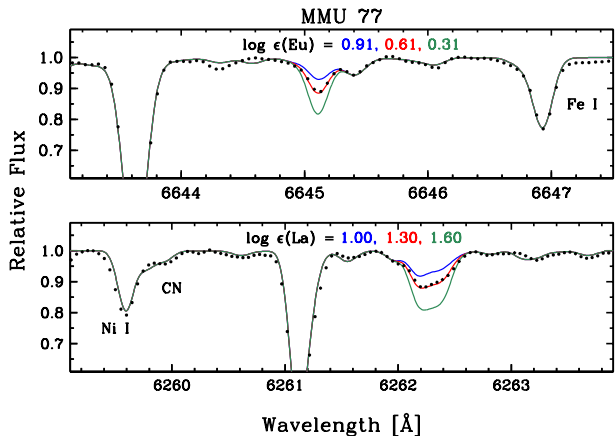


Figure 7. Synthetic and observed spectra comparison of MMU 77 for the 6345.1 Å Eu II and 6262.3 Å La II lines. The observed spectrum is represented by black points. Assumed abundances for the three synthetic spectra are given in the figure legend. The best fit to the observed spectrum is given with a red solid line. The 0.3 dex lower and upper deviations from the adopted abundance are represented with green and blue solid lines, respectively.

the spectral gap between the echelle orders, it was taken into account whenever it was available. The scatter in Zn abundances, determined from only the Zn I line at 6362.3 Å, is mainly caused by CN and other atomic contaminants in this region.

Most of our Fe-group abundances are in good agreement with those of Red12 and Car11, except for the two reverse solar analysis species, VI and Co I. Although the relative deficiencies that we found in Mn and Cu may be real, we repeat our cautions that recent lab studies concerning these elements are unavailable. For V, the discrepancies are $\Delta[\text{V}/\text{Fe}]_{\text{R}} \equiv 0.13$, $\Delta[\text{V}/\text{Fe}]_{\text{C}} \equiv 0.11$ and for Co, $\Delta[\text{Co}/\text{Fe}]_{\text{R}} \equiv 0.10$, $\Delta[\text{Co}/\text{Fe}]_{\text{C}} \equiv 0.13$. For Mn, $\Delta[\text{Mn}/\text{Fe}]_{\text{R}} \equiv 0.10$. And for Zn, $\Delta[\text{Zn}/\text{Fe}]_{\text{R}} \equiv 0.12$. The mean Sc abundance is in good agreement with both Red12 and Car11.

Neutron-capture elements: We applied synthetic spectrum analyses to three so-called *s*-process (slow neutron-capture) elements Y, La, Nd, and one *r*-process (rapid neutron-capture) element Eu. We also tried to derive Ba abundances in our stars. Unfortunately, all Ba II lines are saturated in most of our target stars. Abundances derived from Ba lines are very sensitive to damping, microturbulence, and the outer atmosphere structures of our stars. Given these difficulties, we decided to discard Ba from our element list. Three Eu II and four La II lines were used to determine their abundances. In Figure 7, one of the regions for Eu II and one for La II are illustrated for MMU 77. We show three different syntheses with assumed abundances that are separated by 0.3 dex, with the middle (red color) synthetic spectrum having the abundance that best fits the observed feature. The synthetic line profiles of these features clearly match the details of the observed lines.

All *n*-capture element abundances are in good agreement with those of Red12 and Car11 within the mutual uncertainties, except for $\Delta[\text{Nd II}/\text{Fe}]_{\text{R}} \equiv -0.12$ and $\Delta[\text{Nd II}/\text{Fe}]_{\text{C}} \equiv 0.16$. The difference may be caused by the different analytical methods used in each study.

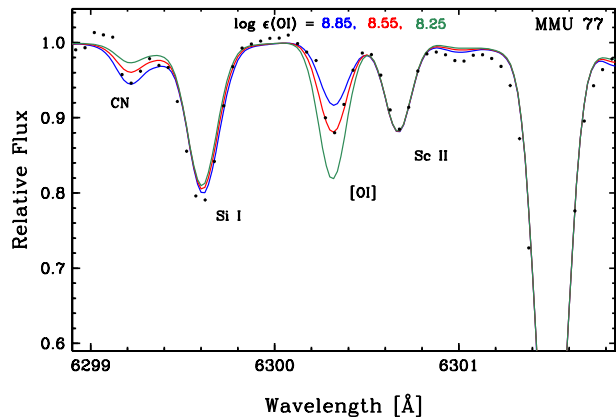


Figure 8. Synthetic and observed spectrum comparison of MMU 77 for the [O I] 6300.3 Å line. Lines and symbols are equivalent to those in Fig. 7.

6.2 Proton-capture elements

We employed full synthetic spectrum computations to study all features of the LiCNO abundance group. Using the new molecular laboratory data summarized in §4.1, we were able to derive accurate CNO abundances for the stars in our sample. The elements C, N, and O are interdependent through their coupling into molecules such as CN, CH, and especially CO. Therefore, their abundances must be determined iteratively, performing molecular equilibrium computations at all steps. For each star we started our iterations by deriving the O abundances first from the [O I] 6300.3 Å line. Then, C abundances were determined from CH features located around 4311 Å and 4325 Å, and C₂ bands at 5160 Å and 5631 Å region. Finally for the N abundances, we used ¹²CN and ¹³CN red system lines in the 7995–8040 Å region. This process was applied until the changes in element abundances were negligible from iteration to iteration.

In Figures 8, 9 and 10, we give examples of synthetic-to-observed spectrum matching for CNO regions of MMU 77. Figure 8 illustrates the determination of O abundances from the [O I] (6300.30 Å) line. The feature is blended with both Ni I (6300.34 Å) and CN (6300.27 Å). We tried to account for these contaminants carefully (see Sneden et al. 2014 for details). Transition probabilities of Johansson et al. (2003) were used for the Ni I line. We derived C abundances from several molecular band regions: the CH G-band, and the C₂ (0–0) bandhead at 5155 Å and the (0–1) bandhead at 5635 Å. In Figure 9, we give a portion of CH G-band in panel (a). The two bandheads for C₂ are illustrated in panels (b) and (c). The complex structures of these molecular regions lead to fluctuating C abundances from star to star, but they still remained within error limits. Final C abundances were calculated by taking an average of the values obtained from these molecular regions. Figure 10 shows an example of N abundance synthesis from the CN region. An average was taken to obtain final N abundances.

To our knowledge, the C and N abundances derived here are the first for NGC 752 members. In standard stellar evolution, the mean N abundance is expected to increase and the C abundance decrease by the RGB evolutionary phase. Our derived C and N abundances follow this trend. However, our O abundances exhibit a subsolar abun-

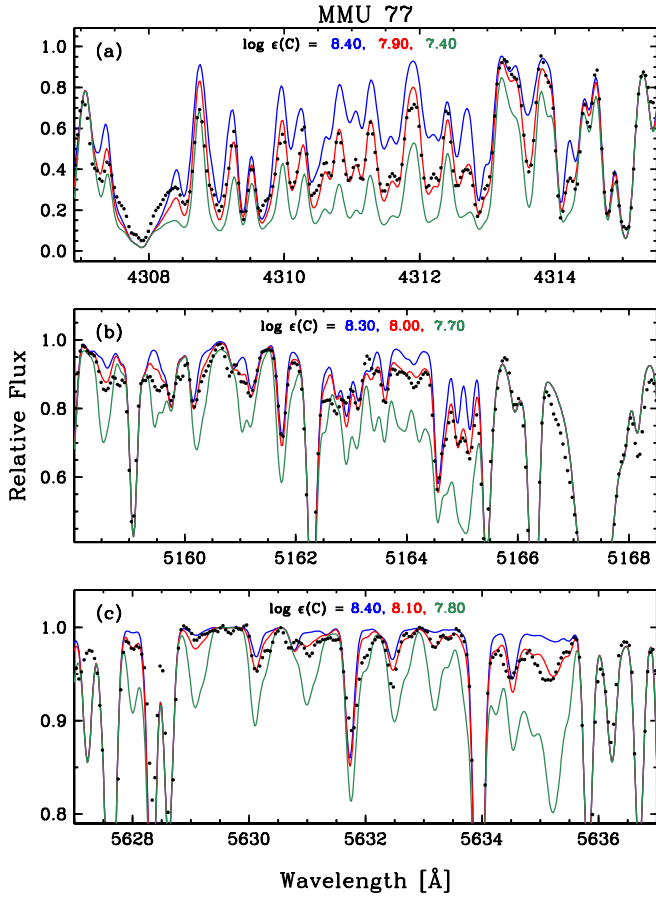


Figure 9. Synthetic and observed spectra of three wavelength regions used for C abundance determination. A portion of the CH G-band (panel a), C₂ (0–0) bandhead at 5155 Å (panel b) and C₂ (0–1) bandhead at 5635 Å (panel c) are illustrated. Lines and symbols are as in Figure 7.

dance. This is in disagreement with the invariance of solar normalized O abundances suggested by classical stellar evolution. Car11 determined O abundances from the same forbidden line and found $[O/Fe]=0.03 \pm 0.04$. However, unlike our study, they did not take into account the interdependence of C, N and O abundances while determining the oxygen abundances. Furthermore, they found somewhat higher surface gravities (see §5.4). These two effects essentially account for the discrepancy from our result of $[O/Fe]=-0.18 \pm 0.04$. Recently, Maderak et al. (2013) reported an average $[O/Fe]=-0.02$ abundance for the cluster, which was determined from the main-sequence members of NGC 752 using 7774 Å–O I triplet region. Taking into account the non-LTE abundance corrections for oxygen triplet (up to almost 0.2 dex, e.g., Ecuivillon et al. 2006), Maderak’s non-LTE $[O/Fe]$ abundance is found to be around -0.22 dex, which is in agreement with the oxygen abundance range we report in Table 10 and also illustrate in Figure 6.

In Figure 11 we plot the derived CNO abundances as functions of T_{eff} for our 10 NGC 752 programme stars. This plot reveals no obvious trend with T_{eff} , and there are none to be found with the other model atmosphere parameters.

¹²C/¹³C: ¹²CN and ¹³CN features that can be used for ¹²C/¹³C determination are located throughout the red spec-

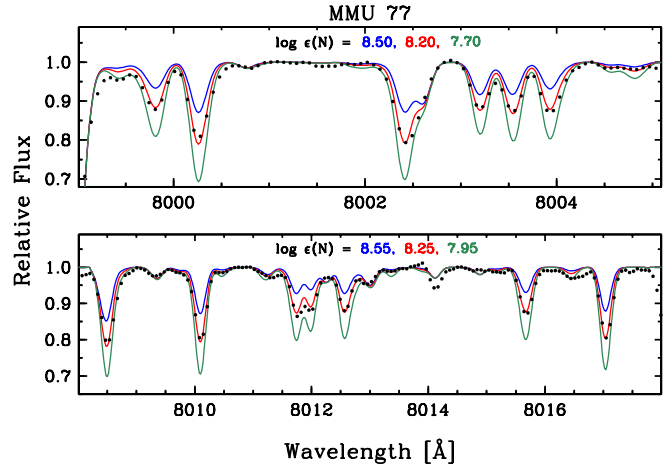


Figure 10. A portion of synthetic and observed spectral regions with CN absorption features used for N abundance determination. Lines and symbols are as in Figure 7.

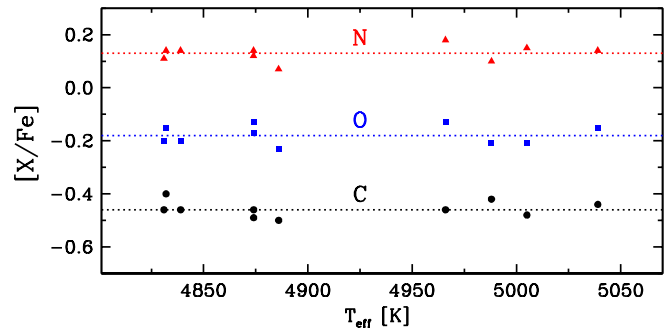


Figure 11. Distribution of C, N and O abundances plotted versus the effective temperatures for RG members.

tral domain. The most useful ones for our spectral coverage are in the ~ 8000 – 8048 Å region. Although there are several available features, we decided to determine ¹²C/¹³C values from the ratio of ¹²CN at 8003.5 Å to ¹³CN at 8004.6 Å due to severe line blending in other features. In Figure 12, we give an example of different assumed ¹²C/¹³C ratios matched to this feature for two members of NGC 752. We list all ¹²C/¹³C ratios for our sample and the ratios gathered from the literature in Table 11. The ¹²C/¹³C ratios determined for our targets range between 13 and 25. Gil89 derived ¹²C/¹³C for six members of NGC 752, but later two of them were found to be spectroscopic binaries by Mer08. The main differences between Gil89 and our work are that we have higher spectral resolution and ¹²C/¹³C ratios were determined during the iterative process that we obtained CNO abundances, and therefore they should be more reliable. Our results indicate that two of the RGs, MMU 1 and MMU 77 have ¹²C/¹³C = 25 while Gil89 found lower values: ¹²C/¹³C = 17 for MMU 1 and ¹²C/¹³C = 16 for MMU 77. For the other shared RGs, MMU 295 and MMU 311, there is better agreement: we found ¹²C/¹³C = 20 and 15, respectively, while Gilroy reported ¹²C/¹³C = 16 for both members.

Li: We derived Li abundances from the neutral Li 6707.8 resonance doublet, which is somewhat blended with Fe I line at 6707.4 Å. Hyper-fine structure of the resonance doublet was also taken into account. An example

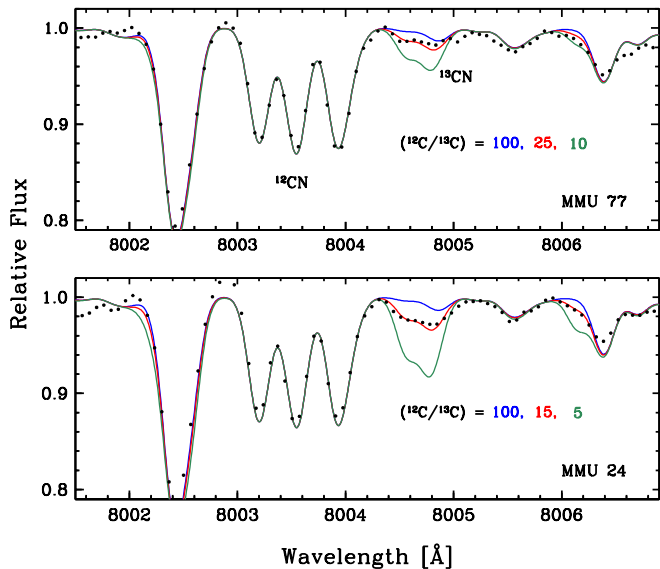


Figure 12. Comparison of synthetic and observed spectra of MMU 77 and 24 for the observed CN features around 8004 Å. These two stars represent the highest and lowest $^{12}\text{C}/^{13}\text{C}$ ratios in our sample. Lines and symbols are as in Figure 7.

of synthetic/observed spectrum comparison is given in Figure 13. As seen in this figure, Li abundances vary greatly from star to star. We were able to measure Li abundances for RGs such as MMU 77 and MMU 311 (top two panels of Figure 13), while RGs such as MMU 137 (bottom panel) does not have a detectable Li feature ($\log \epsilon < 0$). As tabulated in Table 11, the star-to-star abundance range is very large, more than 1.4 dex. The strongest Li was detected in MMU 77 with an abundance of $\log \epsilon = 1.34$. For the same member, Pil86 and Gil89 also determined Li abundances using the same resonance line and found $\log \epsilon = 1.1$ and 1.4, respectively. We could not detect Li in MMU 295, and neither could Pil86 ($\log \epsilon < +0.5$) but Gil89 reported a detection and with $\log \epsilon = 0.45$. Our non-detection is to be preferred as it is based on higher-quality spectra.

7 DISCUSSION AND CONCLUSIONS

This NGC 752 study is the first of a series of papers presenting the results of chemical abundance analysis and investigating the evolutionary status of the RG members of OCs. Our main focus was the abundances of the key elements of LiCNO p -capture group to help us understand the evolutionary stages of the stars and to reveal the discrepancies among RG members.

Before starting with the analysis process, we first confirmed cluster membership of the 10 selected RGs in NGC 752 by deriving new RV values. Since important parameters such as reddening, distance modulus, and turnoff mass are readily available for clusters such as NGC 752, we were able to calculate relatively accurate initial parameters for each star. To derive the most accurate atmospheric parameters, we made a significant effort to establish the initial parameters prior to detailed spectrum analysis. Initial effective temperatures were determined by taking the average of three different temperatures calculated from the $(B - V)$,

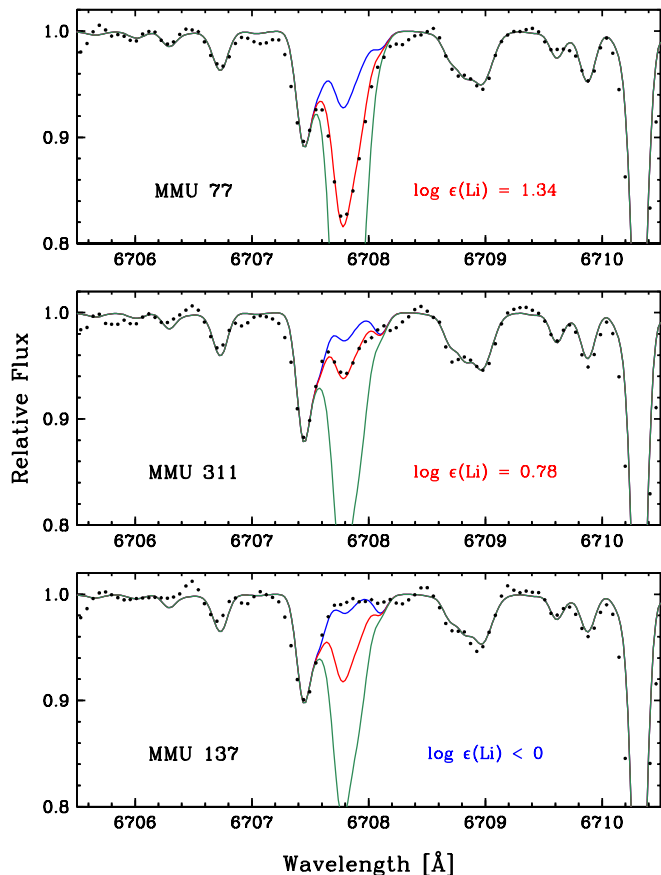


Figure 13. Comparison of synthetic and observed spectra of MMU 77, 311 and 137 for 6707.8 Å Li line. These three stars represent the diversity in Li abundances among the RGs of NGC 752. Lines and symbols are as in Figure 7.

$(V - K)$ colors and line depth ratios of the temperature sensitive species. We calculated initial $\log g$ values using the formula described in §5.2, and also estimated an initial metallicity of $[\text{Fe}/\text{H}] = 0$. Then, we derived final model atmosphere parameters T_{eff} , $\log g$, ξ_t and $[\text{Fe}/\text{H}]$ by using both neutral and ionized species of Fe and Ti. The model atmospheres of the individual RG members (Table 6) yielded an average cluster metallicity of about solar, $\langle [\text{M}/\text{H}] \rangle = -0.07$.

We derived the abundances of a number of elements including the light (Li, C, N, O), odd-Z (Na, Al), α (Mg, Si, Ca), Fe-group (Ti, Cr, Ni, Mn, Cu, Zn) and n -capture elements (Y, La, Nd, Eu). We derived $^{12}\text{C}/^{13}\text{C}$ ratios of the RGs by employing the synthetic spectrum fitting to the ^{12}CN and ^{13}CN features located around 8004 Å. The elemental abundances are mostly scattered around solar values as seen in Figure 6. From that figure, it is obvious that species such as Cu, Mn, and Nd exhibit more scatter due to either lack of updated gf values or complex hyper-fine structure. However, the overall abundance consistency among all RG members of NGC 752 indicates that they all share the same origin. Recently, Carraro et al. (2014) have reported the abundances of seven RC members in the OC NGC 4337, which is nearly identical to NGC 752 in age and metallicity. The CMDs of these clusters are very similar except that NGC 752 has fewer main sequence stars. NGC 4337 and NGC 752 appear to have differences in the abundances of

Table 11. Lithium abundances, carbon isotopic ratios and probable evolutionary status of NGC 752 RG members.

Star	$\log \epsilon(\text{Li})^a$	$\log \epsilon(\text{Li})^b$	$^{12}\text{C}/^{13}\text{C}^b$	$\log \epsilon(\text{Li})^c$	$^{12}\text{C}/^{13}\text{C}^c$	Evol. Phase
MMU 1	<+0.5	0.45	17	0.15	25	RGB
MMU 3				1.25	25	RGB
MMU 11				1.00	25	RC
MMU 24	<+0.5			<0	15	RC
MMU 27				0.95	17	RC
MMU 77	1.1	1.40	15.5	1.34	25	RGB
MMU 137	<+0.3			<0	15	RC
MMU 295	<+0.5	0.25	16	<0	20	RHB
MMU 311	<+0.3	0.77	16	0.78	20	RC
MMU 1367				<0	17	RC

^a Pilachowski et al. (1988)

^b Gilroy (1989)

^c This study

some species. For example, Carraro et al. report that Na, V and Co are overabundant and Zn is underabundant in NGC 4337, while we find that they have almost solar abundances in NGC 752. CNO abundances in both OCs indicate that the observed members are certainly evolved. However, C and O abundances are deficient in NGC 752, while N is more abundant in NGC 4337. These differences suggest that both clusters might have somewhat different chemical origin. Further study of these species in both clusters is needed to explain and explore these differences in greater detail.

One of the main goals of our study was to derive reliable abundances of the *p*-capture LiCNO abundance group. To our knowledge, our study is the first that reports the C and N abundance patterns of evolved stars in NGC 752. The results show the agreement among the CNO abundances of the individual members, which also indicates a common origin for the NGC 752 cluster member RGs.

The C under-abundances and N over-abundances conform to expectations from classical theory of stellar evolution. *p*-capture reactions are the main mechanisms that govern He-production in the core of a star during the main-sequence and later in the H-burning shell during the RGB evolution. When a star evolves along subgiant branch and becomes a first-ascent RGB star, its outer convective envelope broadens and reaches down to the H-burning shell, eventually dredging the H-processed material up to its surface. This so-called first dredge-up phenomenon carries the signatures of internal mixing up and shows itself via altered abundances in mainly ^{13}C and ^{14}N on the stellar surface (e.g. Iben 1967; Iben & Renzini 1984).

In NGC 752, O is underabundant by about 0.18 dex. However, it is not uncommon to find subsolar oxygen abundances in OCs. We refer the reader to Figure 19 of Yong et al. (2005), who investigate the distribution of [O/Fe] abundances versus age and Galactocentric distances (R_{GC}) of different OC populations in the Galaxy. NGC 752, with an age of 1.6 Gyr and $R_{GC} = 8.3$ kpc (Red12), is similar to many other other OCs with subsolar metallicities and similar Galactocentric distances. We also note the small dispersion among the O abundances of our cluster members. Having the lowest abundance of [O/Fe]=-0.23, MMU 3 has a unique spectroscopic feature for our sample: it shows Ca II

HK emission lines. MMU 77, which has almost the same temperature and gravity as MMU 3, does not carry any signature of Ca II HK emission, and its [O/Fe] = -0.13. As suggested in several studies (e.g. Shchukina et al. 2005), stellar atmospheric inhomogeneities such as granulation may be responsible for the decrease in the oxygen abundances calculated from the forbidden [O I] line at 6300.3 Å. Further investigation of this unusual behavior is beyond the scope of this paper.

According to canonical stellar evolution theories, surface $^{12}\text{C}/^{13}\text{C}$ and Li content can be altered by the end of the first dredge-up after the main sequence and subgiant phases. They are often the main indicators of stellar evolution. We found an unexpectedly large range in both of these abundances in NGC 752 RGs. In our sample, which occupies a relatively small domain of the HR diagram, there are examples that have high $^{12}\text{C}/^{13}\text{C}$ and high Li abundances, indicative of being first-ascent RGBs. There are also cases with low $^{12}\text{C}/^{13}\text{C}$ and Li abundances, indicative of much further evolution, perhaps the post-He-flash RC evolutionary stage. We have only one RG, MMU 295, with no Li feature but $^{12}\text{C}/^{13}\text{C} = 20$. Low $^{12}\text{C}/^{13}\text{C}$ ratios have been used as an extra-mixing indicator for some decades. This explanation dates back at least to Gil89, who found anomalously low isotopic ratios in many RG OC members, and showed an anti-correlation between $^{12}\text{C}/^{13}\text{C}$ and the turnoff mass of a cluster.

Our investigation of NGC 752 light elements benefits from higher spectral resolution, larger sample size, and new molecular data that yields CNO abundances along with Li and $^{12}\text{C}/^{13}\text{C}$. We found low $^{12}\text{C}/^{13}\text{C}$ ratios for only four RGs in in our sample (Table 11). Three of these four also show no detection of Li: MMU 24, 137 and 1367. Such stars are prime suspects for having undergone some extra-mixing processes. However, Li is a fragile element and very sensitive to the details of main sequence stellar envelope conditions. Sestito et al. (2004) have investigated the Li vs. T_{eff} distribution in NGC 752 by studying 18 solar-type members and showed that Li abundance decreases as the temperature of the cluster members decreases. This indicates that the members with slightly different temperatures may have slightly different initial Li abundances.

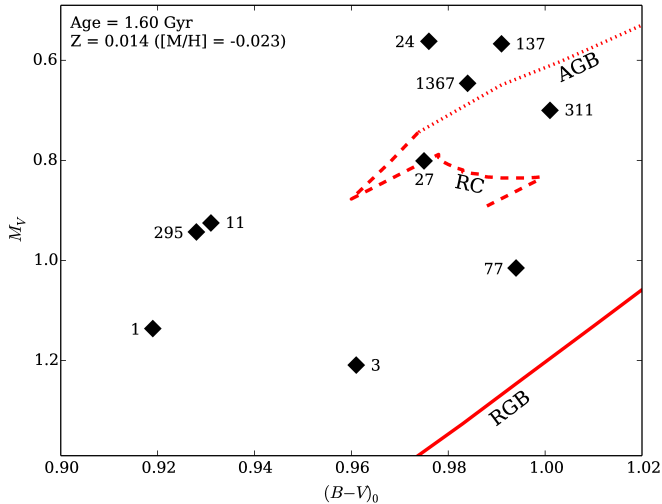


Figure 14. Zoom-in version of the RG region from the CMD given in Figure 1. The RGB, RC and AGB parts of the isochrone are illustrated with (red) solid, dashed and dotted lines, respectively. The points are labeled with the star names.

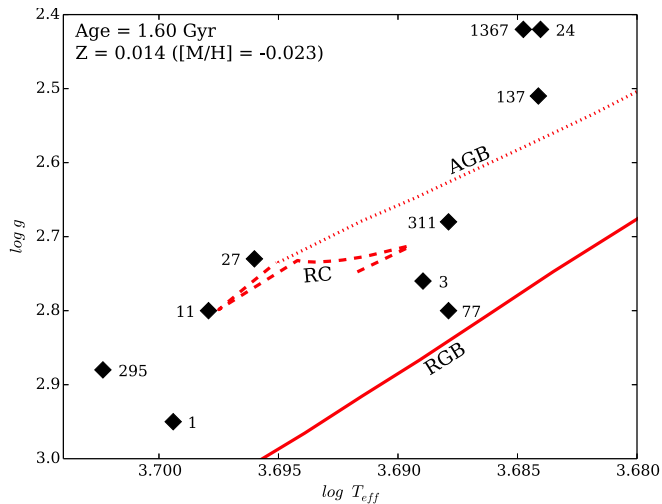


Figure 15. Locations of the RGs in spectroscopic $T_{\text{eff}} - \log g$ diagram. Same PARSEC isochrone is used as described in Figure 1. Symbols and labels are the same as described in Figure 14.

To analyze the light elements among NGC 752 RGs in more detail, we decided to explore the evolutionary status of our RG sample. We re-examined the CMD for NGC 752. We used the photometric data of Dan94, and applied PARSEC isochrones (Bressan et al. 2012), see Figure 1. The best isochrone match to the photometry was found for an age of 1.60 Gyr and metallicity $Z = 0.014$. Figure 14 is a zoomed-in version of the CMD Figure 1, centered on the RGB and RC regions more in detail.

We then used the same isochrone to compare our spectroscopically derived values in the $T_{\text{eff}} - \log g$ plane for the NGC 752 RGs of this study. This comparison, which is independent from the photometric parameters, is displayed in Figure 15. The locations of the targets in the $T_{\text{eff}} - \log g$ diagram are in good agreement with the ones in Figure 14.

By taking into account the locations of our RGs in both Figures 14 and 15, along with the Li abundances and

$^{12}\text{C}/^{13}\text{C}$ ratios derived from the spectral analysis, we tried to estimate the probable evolutionary stages of our programme stars. Our assignments are given in Table 11. The reader should be warned that we do not indicate T_{eff} and $\log g$ uncertainties in Figure 15 for plotting clarity, but they are large enough to blur the distinction between RGB and RC membership in some cases. Therefore, the evolutionary assignments here are not firm conclusions, but rather plausible estimates.

Our reasoning is based on the following observations: (1): MMU 77 lies closer to the RGB than other RGs in both Figure 14 and 15. It also has high Li abundance and carbon isotopic ratio (Table 11). Abundances and CMD location indicate that this star is a regular first-ascent RGB. (2): MMU 24 and MMU 137 present the most obvious examples of post-He-flash RC (or even AGB) stars, as they combine highly evolved positions in Figures 14 and 15 with low $^{12}\text{C}/^{13}\text{C}$ and no Li detection. (3): The CMD location of MMU 311 appears to indicate RC status. However, the intermediate abundance values of $^{12}\text{C}/^{13}\text{C}$ and Li slightly negate this interpretation. We label this star as an RC, but caution is advised in this case. (4): MMU 1 is not easily understood. This star seems to be close to RGB in Figure 15 while it is somewhat more luminous than a true RGB star in Figure 14. It has low Li but high $^{12}\text{C}/^{13}\text{C}$. We believe that MMU 1 is an RGB star, but this assignment is not easy to defend. (5): MMU 295 is the hottest RG in our sample. Therefore, it could possibly be a red horizontal branch (RHB) star. The case for this is strengthened by the star's lack of Li detection and moderate $^{12}\text{C}/^{13}\text{C}$ value of 20. We tentatively suggest that our 10-star NGC 752 RG sample contains three first-ascent RGBs, six RCs and one RHB.

Spectroscopically-derived accurate temperatures, surface gravities, Li abundances and carbon isotopic ratios are among the most important parameters to gain better understanding about the evolutionary stages of the evolved stars. However, matching observed HR Diagram locations of NGC 752 RGs to isochrones is a challenge without knowing stellar masses. We have a good estimate of the NGC 752 turnoff mass due to comparisons of the observed data to both the $\log g - T_{\text{eff}}$ isochrone and the CMD. However, individual cluster members might have slightly different initial masses, which could lead us to observe some diversity among the elemental abundances and $^{12}\text{C}/^{13}\text{C}$ ratios. Internal mixing may have taken place with different efficiencies in these stars. As a result, some of the RGs, especially with low $^{12}\text{C}/^{13}\text{C}$ ratios, may have experienced extra-mixing on the RGB after the 1st dredge-up, which takes place when low-mass stars reach the so-called luminosity-function bump. (Gratton et al. 2000; Charbonnel & Lagarde 2010).

Consequently, RGs are important for understanding how chemical evolution effects cluster stars. Additionally, they also provide excellent opportunities to investigate effective mixing processes via their $^{12}\text{C}/^{13}\text{C}$ ratios. We will present more results that will investigate the chemical evolution of the RG members of several OCs in future papers.

ACKNOWLEDGMENTS

Major parts of this research occurred during several exchange visits among the authors at the Department of As-

tronomy and Space Sciences of Ege University and the Department of Astronomy of the University of Texas at Austin. We thank the people of both departments for their hospitality and encouragement of this study. Our work has been supported by The Scientific and Technological Research Council of Turkey (TÜBİTAK, project No. 112T929), by the US National Science Foundation (NSF, grants AST 09-08978 and AST 12-11585), and by the University of Texas Rex G. Baker, Jr. Centennial Research Endowment. This research has made use of NASA's Astrophysics Data System Bibliographic Services; the SIMBAD database and the VizieR service, both operated at CDS, Strasbourg, France. This research has made use of the WEBDA database, operated at the Department of Theoretical Physics and Astrophysics of the Masaryk University and of the VALD database, operated at Uppsala University, the Institute of Astronomy RAS in Moscow, and the University of Vienna. We would like to thank to anonymous referee for his/her helpful discussions and careful review of the manuscript.

REFERENCES

- Afşar M., Sneden C., For B. Q., 2012, *AJ*, 144, 20
- Anthony-Twarog B. J., Twarog B. A., 2006, *PASP*, 118, 358
- Asplund M., Grevesse N., Sauval A. J., Scott P., 2009, *ARA&A*, 47, 481
- Bartašiūtė S., Deveikis V., Straižys V., Bogdanovičius A., 2007, *Balt. Astron.*, 16, 199
- Bartašiūtė S., Janusz R., Boyle R. P., Philip A. G. D., 2011, *Balt. Astron.*, 20, 27
- Biazzo K., Frasca A., Catalano S., Marilli E., 2007a, *Astron. Nachr.*, 328, 938
- Biazzo K. et al., 2007b, *A&A*, 475, 981
- Boothroyd A. I., Sackmann I. J., 1999, *ApJ*, 510, 232
- Bressan A., Marigo P., Girardi L., Salasnich B., Dal Cero C., Rubele S., Nanni A., 2012, *MNRAS*, 427, 127
- Brooke J. S. A., Bernath P. F., Schmidt T. W., Bacskay G. B., 2013, *JQSRTJ. Quant. Spectrosc. Radiat. Transfer*, 124, 11
- Brooke J. S. A., Ram R. S., Western C. M., Li G., Schwenke D. W., Bernath P. F., 2014, *ApJS*, 210, 23
- Brugamyer E., Dodson-Robinson S. E., Cochran W. D., Sneden C., 2011, *ApJ*, 738, 97
- Caffau E., Ludwig H. G., Steffen M., Ayres T. R., Bonifacio P., Cayrel R., Freytag B., Plez B., 2008, *A&A*, 488, 1031
- Carraro G., Monaco L., Villanova S., 2014, *A&A*, 568, A86
- Carrera R., Pancino E., 2011, *A&A*, 535, A30 (Car11)
- Castellani V., Chieffi A., Straniero O., 1992, *ApJS*, 78, 517
- Castelli F., Kurucz R. L., 2003, in N. Piskunov, W.W. Weiss, D.F. Gray, eds, *Modelling of Stellar Atmospheres*. IAU Symposium, Vol. 210, p. 20P
- Charbonnel C., 1994, *A&A*, 282, 811
- Charbonnel C., Lagarde N., 2010, *A&A*, 522, A10
- Charbonnel C., Brown J. A., Wallerstein G., 1998, *A&A*, 332, 204
- Daniel S. A., Latham D. W., Mathieu R. D., Twarog B. A., 1994, *PASP*, 106, 281 (Dan94)
- Dearborn D. S. P., Eggleton P. P., Schramm D. N., 1976, *ApJ*, 203, 455
- Delbouille L., Roland G., Neven L., 1973, *Atlas photometrique DU spectre solaire de λ 3000 a λ 10000*. Cointe-Ougree, Belgium : Institut d'Astrophysique de l'Universite de Liege, 1973
- Ebbighausen E. G., 1939, *ApJ*, 89, 431
- Ecuvillon A., Israelian G., Santos N. C., Shchukina N. G., Mayor M., Rebolo R., 2006, *A&A*, 445, 633
- Fitzpatrick M. J., 1993, in R.J. Hanisch, R.J.V. Brissenden, J. Barnes, eds, *Astronomical Data Analysis Software and Systems II*. Astronomical Society of the Pacific Conference Series, Vol. 52, p. 472
- Gilroy K. K., 1989, *ApJ*, 347, 835 (Gil89)
- Gilroy K. K., Brown J. A., 1991, *ApJ*, 371, 578
- Girardi L., Mermilliod J. C., Carraro G., 2000, *A&A*, 354, 892
- Gratton R. G., Sneden C., Carretta E., Bragaglia A., 2000, *A&A*, 354, 169
- Gray D. F., Brown K., 2001, *PASP*, 113, 723
- Gray D. F., Johanson H. L., 1991, *PASP*, 103, 439
- Heinemann K., 1926, *Astron. Nachr.*, 227, 193
- Heiter U., Soubiran C., Netopil M., Paunzen E., 2014, *A&A*, 561, A93
- Hinkle K., Wallace L., 2005, in T.G. Barnes III, F.N. Bash, eds, *Cosmic Abundances as Records of Stellar Evolution and Nucleosynthesis*. Astronomical Society of the Pacific Conference Series, Vol. 336, p. 321
- Hinkle K. H., Wallace L., Ram R. S., Bernath P. F., Sneden C., Lucatello S., 2013, *ApJS*, 207, 26
- Hollek J. K., Frebel A., Roederer I. U., Sneden C., Shetrone M., Beers T. C., Kang S. j., Thom C., 2011, *ApJ*, 742, 54
- Iben I., Renzini A., 1984, *Phys. Rep.*, 105, 329
- Iben Jr. I., 1967, *ApJ*, 147, 624
- Iglesias C. A., Rogers F. J., 1996, *ApJ*, 464, 943
- Johansson S., Litzén U., Lundberg H., Zhang Z., 2003, *ApJL*, 584, L107
- Kupka F. G., Ryabchikova T. A., Piskunov N. E., Stempels H. C., Weiss W. W., 2000, *Baltic Astronomy*, 9, 590
- Kurucz R. L., 2011, *Can. J. Phys.*, 89, 417
- Kurucz R. L., Furenlid I., Brault J., Testerman L., 1984, *Solar flux atlas from 296 to 1300 nm*
- Lambert D. L., Ries L. M., 1981, *ApJ*, 248, 228
- Lawler J. E., Dakin J. T., 1989, *J. Opt. Soc. Am. B.*, 6, 1457
- Lobel A., 2011, *Can. J. Phys.*, 89, 395
- Luck R. E., 1994, *ApJS*, 91, 309
- Maderak R. M., Deliyannis C. P., King J. R., Cummings J. D., 2013, *AJ*, 146, 143
- Maeder A., Meynet G., 1991, *A&ASS*, 89, 451
- Marigo P., 2001, *A&A*, 370, 194
- Marigo P., Aringer B., 2009, *A&A*, 508, 1539
- Masseron T. et al., 2014, *A&A*, 571, A47
- Mermilliod J. C., Mathieu R. D., Latham D. W., Mayor M., 1998, *A&A*, 339, 423
- Mermilliod J. C., Mayor M., Udry S., 2008, *A&A*, 485, 303 (Mer08)
- Meynet G., Mermilliod J. C., Maeder A., 1993, *A&ASS*, 98, 477
- Mikolaitis Š., Tautvaišienė G., Gratton R., Bragaglia A., Carretta E., 2010, *MNRAS*, 407, 1866
- Mikolaitis Š., Tautvaišienė G., Gratton R., Bragaglia A., Carretta E., 2011a, *MNRAS*, 413, 2199

- Mikolaitis Š., Tautvaišienė G., Gratton R., Bragaglia A., Carretta E., 2011b, MNRAS, 416, 1092
- Mikolaitis Š., Tautvaišienė G., Gratton R., Bragaglia A., Carretta E., 2012, A&A, 541, A137
- Moore C. E., Minnaert M. G. J., Houtgast J., 1966, The solar spectrum 2935 Å to 8770 Å
- O'Brian T. R., Wickliffe M. E., Lawler J. E., Whaling W., Brault J. W., 1991, J. Opt. Soc. Am. B., 8, 1185
- Paunzen E., Heiter U., Netopil M., Soubiran C., 2010, A&A, 517, A32
- Pilachowski C., 1986, ApJ, 300, 289
- Pilachowski C., Saha A., Hobbs L. M., 1988, PASP, 100, 474
- Pöhl H., Paunzen E., 2010, A&A, 514, A81
- Ram R. S., Brooke J. S. A., Bernath P. F., Sneden C., Lucatello S., 2014, ApJS, 211, 5
- Ramírez I., Meléndez J., 2005, ApJ, 626, 465
- Reddy A. B. S., Giridhar S., Lambert D. L., 2012, MNRAS, 419, 1350 (Red12)
- Roederer I. U., Sneden C., Thompson I. B., Preston G. W., Shectman S. A., 2010, ApJ, 711, 573
- Roederer I. U., Preston G. W., Thompson I. B., Shectman S. A., Sneden C., Burley G. S., Kelson D. D., 2014, AJ, 147, 136
- Rogers F. J., Iglesias C. A., 1992, ApJ, 401, 361
- Sestito P., Randich S., Pallavicini R., 2004, A&A, 426, 809
- Shchukina N. G., Trujillo Bueno J., Asplund M., 2005, ApJ, 618, 939
- Skrutskie M. F. et al., 2006, AJ, 131, 1163
- Smiljanic R., Gauderon R., North P., Barbuy B., Charbonnel C., Mowlavi N., 2009, A&A, 502, 267
- Sneden C., 1973, ApJ, 184, 839
- Sneden C., Pilachowski C. A., 1986, ApJ, 301, 860
- Sneden C., Pilachowski C. A., Vandenberg D. A., 1986, ApJ, 311, 826
- Sneden C., Lucatello S., Ram R. S., Brooke J. S. A., Bernath P., 2014, ApJS, 214, 26
- Strassmeier K. G., Schordan P., 2000, Astron. Nachr., 321, 277
- Sweigart A. V., Mengel J. G., 1979, ApJ, 229, 624
- Sweigart A. V., Greggio L., Renzini A., 1989, in Bulletin of the American Astronomical Society. Vol. 21, p. 789
- Tautvaišienė G., Edvardsson B., Tuominen I., Ilyin I., 2000, A&A, 360, 499
- Tautvaišienė G., Edvardsson B., Puzeras E., Ilyin I., 2005, A&A, 431, 933
- Tomkin J., Lambert D. L., Luck R. E., 1975, ApJ, 199, 436
- Tomkin J., Luck R. E., Lambert D. L., 1976, ApJ, 210, 694
- Torres G., 2010, AJ, 140, 1158
- Torres G., Fischer D. A., Sozzetti A., Buchhave L. A., Winn J. N., Holman M. J., Carter J. A., 2012, ApJ, 757, 161
- Tull R. G., MacQueen P. J., Sneden C., Lambert D. L., 1995, PASP, 107, 251
- Vandenberg D. A., Bergbusch P. A., Dowler P. D., 2006, ApJS, 162, 375
- Wallace L., Hinkle K. H., Livingston W. C., Davis S. P., 2011, ApJS, 195, 6
- Yong D., Carney B. W., Teixeira de Almeida M. L., 2005, AJ, 130, 597